Spring 2011

Continuous low thrust for small spacecraft proximity operations

James Harris Meub

Department: Mechanical and Aerospace Engineering

CONTINUOUS LOW THRUST FOR SMALL SPACECRAFT PROXIMITY OPERATIONS

by

JAMES HARRIS MEUB

A THESIS

Presented to the Faculty of the Graduate School of the

MISSOURI UNIVERSITY OF SCIENCE AND TECHNOLOGY

In Partial Fulfillment of the Requirements for the Degree

MASTER OF SCIENCE IN AEROSPACE ENGINEERING

2011

Approved by

Henry Pernicka, Advisor
S.N. Balakrishnan
Serhat Hosder

ABSTRACT

Recently, both DoD and NASA have demonstrated increased interest in the development of close proximity operations for space systems. AFRL's Advanced Sciences and Technology Research Institute for Astrodynamics (ASTRIA) has defined several key research topics relevant to military priorities, with one area of critical importance being the inspection and observation of low Earth orbit resident space objects (RSOs). This study investigates the feasibility of using a low-thrust cold-gas propulsion system to effectively and accurately facilitate resident space object inspection. Specifically, this study focuses on the Missouri S&T Satellite mission (M-SAT) as a means to demonstrate autonomous RSO inspection. This paper describes the mission requirements and outlines a mission plan for spacecraft separation, formation stabilization, and RSO circumnavigation over a 1.5 orbital period time frame. Autonomous guidance path design and comparisons of multiple feedback control systems are developed as a preliminary investigation in support of the M-SAT mission. The effects of data corruption with measurement and process noise on the mission success criteria are also investigated to determine the performance requirements of the onboard state sensors. The results presented provide a basis for simulating the M-SAT mission from separation to extended mission operations. Velocity change and fuel consumption rates are provided for future mission design and requirement verification.

ACKNOWLEDGMENTS

For my father, Daniel W. Meub (1924 – 2011). You taught me to be a lifelong student, and to take copious notes. You taught me that knowledge, equality, culture, and compassion are the most essential gifts that we can give to each other. I will miss your guidance, wisdom and advice. My hope is to live life half as well as you did. I will do my best to make you proud.

The author would like to thank his loving, supportive, and beautiful wife for always being there for him, even when he spent far too much time in the lab. I couldn't have done it without you.

The author would like to thank his mother. Thank you for teaching me that hard work is always worth the reward and for understanding when I moved halfway across the country to pursue my dream.

The author would like to thank his advisor, Dr. Pernicka, for (hopefully) letting him graduate. Thank you for giving me guidance and direction over the past 6 years. You are a good friend and wonderful mentor.

Dr. Balakrishnan and Dr. Hosder were excellent in providing me the skills to conduct this research. Their knowledge of control systems, state estimation, and numerical methods was instrumental in enabling my success at Missouri S&T.

Special thanks to Mike Dancer, Jason Searcy, Nathan Harl, and Shawn Miller for setting me straight when I got off track, whether by talking through a technical issue or personal one.

Thank you to the entire M-SAT team for providing me with an awesome platform to do research on, I've become a better engineer by being around all of you. Good luck in NS-7, hopefully this research will help us win.

The NASA Missouri Space Grant Consortium was instrumental in providing me the funding to begin this line of research.

TABLE OF CONTENTS

LIST OF ILLUSTRATIONS

LIST OF TABLES

NOMENCLATURE

Symbol	Definition
a	Semimajor Axis
D	Circumnavigation Distance
e	Eccentricity
E	State Error Vector
H	Atmospheric Scale Height
i	Inclination
J	LQR/SDRE Cost Function
J_2	Earth Second-Order Zonal Harmonic
K	LQR/SDRE Controller Gain
L	Spacecraft Latitude
Q	LQR/SDRE State Error Cost
$\hat{r}$	Radial Unit Vector in LVLH Frame
R	LQR/SDRE Control Cost
R_E	Equatorial Radius of the Earth
R_M	Mean Earth-Luna Distance
R_S	Mean Earth-Sol Distance
R_ϕ	Satellite Position Matrix
R_ω	Earth Rotation Matrix
u	LQR/SDRE Control Acceleration
$\hat{v}$	Velocity Unit Vector in LVLH Frame
V_{REL}	Spacecraft Velocity Magnitude Relative to Earth
x	X-axis Position in ECEF Frame
$\dot{x}$	X-axis Velocity in ECEF Frame
$\ddot{x}$	X-axis Acceleration in ECEF Frame
y	Y-axis Position in ECEF Frame
$\dot{y}$	Y-axis Velocity in ECEF Frame
$\ddot{y}$	Y-axis Acceleration in ECEF Frame
z	Z-axis Position in ECEF Frame

$\dot{z}$	Z-axis Velocity in ECEF Frame
$\ddot{z}$	Z-axis Acceleration in ECEF Frame
β	Spacecraft Ballistic Coefficient
ϑ	Inspection Path Segmentation Angle Factor
Λ	Magnitude of Spacecraft Position Vector
μ_E	Gravitational Parameter of Earth
μ_M	Gravitational Parameter of Luna
μ_S	Gravitational Parameter of Sol
ν	True Anomaly
ρ_o	Atmospheric Density at Sea Level
ω	Argument of Periapsis
Ω	Right Ascension of the Ascending Node

1. INTRODUCTION

1.1. BACKGROUND

Satellite formation flight and, more specifically, resident space object inspection has become a topic of increasing interest in recent years. The ability to characterize the functionality, capabilities and health of “uncooperative” and “non-cooperative” spacecraft is a desired goal of both the military and scientific communities. Satellites known as “inspector spacecraft” are desired that provide real-time information and imaging of on-orbit satellites or objects in order to meet these goals. Inspector spacecraft can be launched with an array of imaging and navigation devices used to inspect and analyze the size, shape, rotation rate, health, external equipment and possible damaged areas of a resident space object. Inspector spacecraft are required to perform these inspections by circumnavigation, relative fixed point imaging, and station keeping about a resident space object or target satellite.

Spacecraft proximity operations are subdivided into two categories: cooperative and non-cooperative. Cooperative RSO inspection may involve missions which are primarily of a scientific or mutually beneficial nature. Goals of cooperative space object inspection include satellite servicing, rendezvous, refueling, EVA planning, and heat shield integrity verification. Examples of previous successful missions which involved cooperative spacecraft proximity operations are primarily found in manned spaceflight. The Gemini missions were the first to investigate satellite separation and recapture. The Apollo missions built on the success of cooperative non-autonomous proximity operations. More recently, human controlled docking of both the Soyuz capsule and Space Shuttle was accomplished at MIR and the International Space Station. Typically a computer controlled guidance program is operational and provides detailed range and range rate information to the pilot during such maneuvers. It is assumed that cooperative RSO position and velocity at any given time are known within some error bounds and that these position and velocity estimates are known at all times. For the current study, the RSO is *not* assumed to be cooperative.

Non-cooperative and uncooperative RSO inspection occurs when the target spacecraft is not actively transmitting position or velocity data to the inspector spacecraft.

These scenarios may involve spacecraft that are in some way incapacitated or inoperative (non-cooperative) and those "adversarial" RSOs that intentionally do not communicate with the inspector spacecraft (uncooperative). Non/uncooperative RSO inspection may also involve inspection of a spacecraft that is performing an on-orbit thrusting maneuver, requiring the inspector spacecraft to rapidly and autonomously alter the inspection path, inspection distance or other parameters to avoid collision. A non/uncooperative inspection may focus on the detailing of RSO function, capabilities, size, rotation rates, and health. Non/uncooperative inspection is usually assumed to involve visual navigation via imaging or a ranging sensor mounted on the inspection spacecraft. The added difficulty of navigating with imprecise measurement is of future interest and can be modeled by adding white process noise to the simulation model. This method of simulating deficient or imprecise measurement sensors is employed in this paper.

The Missouri S&T Satellite mission focuses on demonstrating non/uncooperative RSO inspection using two spacecraft. The Missouri-Rolla Satellite (MR SAT) and Missouri-Rolla Second Satellite (MRS SAT) are used to improve the Technology Readiness Level of a proximity operations control package and specific hardware configuration in order to benefit future proximity operations missions. MR SAT will obtain relative distance and direction information from an optical camera located on board. The noisy data will then be processed and utilized to perform a circumnavigation of MRS SAT in order to obtain images from multiple perspectives. The goal of this study is to determine the circumnavigation path, control schemes, and maximum measurement noise allowable by the visual navigation system.

The M-SAT mission may be affected by other error sources aside from measurement noise. Spacecraft attitude error is a significant contributor to extraneous velocity change. The orbit control algorithms employed on the M-SAT mission rely on accurate spacecraft attitude when commanding the thrusters to fire. Attitude control errors will cause the thrusters to fire in an unintended direction, resulting in nonoptimal acceleration that may need to be corrected with another maneuver. Similarly, alignment errors during thruster integration may also affect the velocity change similarly. The control algorithm assumes the thrusters to be in a specific location and pointing in a specific direction. A pointing direction or mounting error in the thrusters may cause

control accelerations to be inefficient or ineffective. Mitigating the effects of these error sources is beyond the scope of this paper; however, future work in these areas is important to assuring mission success.

1.2. PREVIOUS CONTRIBUTIONS

The history of spacecraft proximity operations can be subdivided into two categories, Manned Proximity Operations (MPO) and Autonomous Proximity Operations (APO). MPOs focus on missions or studies which involve route planning and guidance for spacecraft that are piloted or remotely controlled by an astronaut or human entity. In contrast, APOs focus on spacecraft which utilize self-contained algorithms to observe and estimate states and then use those states to compute and execute a control law.

1.2.1. Manned Proximity Operations. The ability of spacecraft to perform proximity operations and rendezvous with other objects in space has been successfully accomplished since the mid-1960s. In late 1965 the first spacecraft proximity operations, specifically close rendezvous, were accomplished during Gemini 6 and Gemini 7 missions. The Gemini spacecraft maneuvered into local space relative to each other and performed a series of imaging tasks, fly-arounds, and general inspections. Four other Gemini missions flew successfully and performed a series of close rendezvous missions and docking maneuvers. A series of EVAs occurred during the Gemini missions, however, crew transfer between the two spacecraft was not accomplished. The Gemini missions served as a gateway to the Apollo program. The Apollo program focused on crew transfer between a “chaser” and a “target” spacecraft. Visual cues and radar range finding were utilized by pilots to maneuver the Command Module (CM) around and close to the Lunar Excursion Module (LEM), eventually docking and transferring supplies and crew.

More recently, Space Shuttle rendezvous with MIR and the International Space Station (ISS) has involved a combination of autonomous proximity operations and crew controlled approach. Autonomous guidance algorithms control the translation and rotational accelerations when the Space Shuttle is farther than 90 meters away. Within 90 meters, pilots on-board utilize LIDAR, laser range finding, IMUs, and GPS systems to

inform their maneuver choices. Daero[30] describes autonomous guidance control schemes for final approach and rendezvous for the Space Shuttle and other large spacecraft for proximity operations, specifically defining approach corridors and control comparisons. Daero's work emphasizes the shift from manned to autonomously controlled proximity operations.

1.2.2. Autonomous Proximity Operations. Since the late 1990s many militaristic and scientific interests have been invested in space to promote space observation missions. The *Defense Technology Area Plan* (2000)[1] has called for the development of small satellites with the capability to "conduct missions such as diagnostic inspection of malfunctioning satellites through autonomous guidance, rendezvous, and even docking techniques." These proximity operations missions are currently being pursued by NASA, DARPA, and the Air Force's ASTRIA program. Several missions have been launched to demonstrate small satellites with these capabilities. The DART (Demonstration for Autonomous Rendezvous Technology)[2] was a NASA mission launched in April 2005. DART used a series of hydrazine and cold-gas thruster systems to perform an inspection of a Department of Defense (DoD) communications satellite. However, due to a miscalculation of fuel consumption rates and collision avoidance program errors, the DART spacecraft ultimately collided with the target spacecraft, leading to a shortened, and unsuccessful, mission. The DART mission emphasizes the need for both more fuel efficient inspector spacecraft and development of more robust proximity operations plans and inspection paths. More specifically, studies have increasingly focused on designing and manufacturing small satellites (less than 500 kg) to perform these specific duties at low development, fuel, and time costs.

Clohessy and Wiltshire[3] introduced a linearized solution to the relative motion of two spacecraft in close proximity to each other. During their research, several closed-form solutions were found to exist that can provide an inspector spacecraft an invariant manifold which, in the absence of perturbations, requires no control force to maintain.

Past research efforts into formation flying and proximity operations between spacecraft has focused primarily on placing spacecraft on a periodic solution to the Hill-Clohessy-Wiltshire equations. The most common method for assuring this periodic solution is an eccentricity-inclination vector separation between the resident space object

and the inspector spacecraft. D'Amico and Montenbruck[4] describe how impulsive maneuvers executed twice per orbital period can perform adequate station keeping along this invariant manifold.

Alfriend and Schaub[5] expand on this by developing a thrusting schedule to correct drifting orbital elements. Corrections to inclination, eccentricity, ascending node, and semimajor axis were made to successfully keep a satellite on a specific invariant manifold. However, these impulsive maneuvers were predetermined and not based upon measurement readings or real-time relative position data, and instead based upon eliminating errors between mean orbital elements of the target satellite and the follower satellite. Alfriend and Schaub[6] continue to develop a series of initial conditions for satellite formation flight. A set of initial impulses is suggested to place a series of satellites on certain closed paths and then to use a low thrust, gimbaling electric propulsion system to perform orbital maintenance. This maintenance control scheme also focused on correction of mean orbital element errors between the spacecraft.

Armellin et al.[7] describe reconfiguration of satellites in formations using continuous and real time control. The goal of their research was to develop a low-thrust control scheme to minimize propellant usage while successfully reconfiguring satellites within acceptable error bounds. The work focused on satellite formations of three or more satellites, each using its own low thrust system to reconfigure the formation.

This study focuses on exploring control algorithms and path definition for proximity operations and inspection missions. This work will enable future spacecraft, specifically the M-SAT spacecraft, to be developed in order to provide autonomous relative navigation and spacecraft inspection to a non-cooperative RSO.

2. MISSION BACKGROUND

2.1. MISSION GOALS

The M-SAT team is currently participating in the Air Force Research Laboratory's (AFRL) Nanosat 7 competition. The purpose of this competition is to provide eleven universities the funding and guidance to design and build an operational small satellite for future launch. Each university selects a mission that is relevant to DoD and AFRL. The Missouri S&T Satellite Project's (M-SAT) mission is to demonstrate non-cooperative spacecraft inspection of a small spacecraft as an inexpensive method to validate technologies for future missions. The M-SAT mission focuses on flying a pair of spacecraft to demonstrate autonomous guidance and control algorithms, experimental navigation hardware and novel propellants. The M-SAT mission statement reads

> "The objective of the M-SAT mission is to provide in-flight validation of vision-based algorithms for autonomous inspection of a resident space object (RSO). This will be accomplished by flying an inspector satellite, MR SAT, in relative proximity to an uncooperative target, MRS SAT. The verification of relative motion will be accomplished using cooperative GPS measurements from MRS SAT."

The MR SAT spacecraft will utilize a vision-based navigation system to perform an uncooperative inspection of MRS SAT. In order to validate mission operations and to provide redundancy, both spacecraft will be equipped with GPS receivers. The vision-based navigation system is assumed to be less accurate than transmitted GPS data. This inaccuracy is simulated by adding Gaussian white noise to the measurement data, filtering the noisy measurements, and using the estimated states to define the navigation maneuvers and guidance paths.

2.2. MISSION LIMITATIONS

The M-SAT mission is subjected to numerous constraints by the Nanosat competition. The M-SAT mission will most likely launch as a secondary payload. In

most scenarios, the primary payload owners decide whether to accept a secondary spacecraft. As such, the M-SAT mission is limited on spacecraft size, mass, and propellant type. The following sections detail the AFRL imposed and M-SAT imposed restrictions and limitations.

2.2.1. AFRL Restrictions. Limitations on the M-SAT mission are set by AFRL's Nanosat-7 User's Guide. The User's Guide document provides recommended practices and also limits the physical characteristics of the M-SAT spacecraft. Table 2.1 shows the primary restrictions for the M-SAT mission.

Table 2.1: AFRL Imposed Restrictions

Mass (kg)	50
Volume (cm x cm x cm)	50 x 50 x 60
Propulsion Tank Maximum Pressure (kPa)	689.5
Propulsion Tank Maximum Internal Energy (kJ)	19.31

The most notable restriction for this study is the propulsion maximum tank pressure. The tank pressure determines the propellant mass that can be stored on board at launch. Careful utilization of this propellant is critical to mission success.

2.2.2. M-SAT Restrictions. In addition to the AFRL imposed restrictions, the M-SAT team has defined a number of self-imposed restrictions for mission success. These restrictions flow from the M-SAT Requirements Verification Matrix and are set to improve the amount and quality of demonstration data that the spacecraft are able to transmit to the ground for post processing. Table 2.2 shows several of these requirements that pertain to the orbit determination and orbit control systems. The orbit determination requirements for the satellite pair call for orbit determination to be done on board and in such a way to provide accurate (within bounds) estimates of the states. The orbit control requirements define a limit on the maximum deviation from the target path.

Table 2.2. M-SAT Imposed Restrictions

The Orbit system shall determine the position of the spacecraft to ±2 meters in any direction with a goal ±1 meter.
The Orbit system shall provide spacecraft position estimates to the flight control system at a frequency of 20 Hz.
The Orbit system shall provide commands capable of maintaining the spacecraft position to within ±5 meters with a goal of ±3 meters.
The Orbit system shall provide control commands at a frequency of 10 Hz.

Exceeding the path deviation over the requirement results in mission failure. The orbit determination limitations are used to assess the maximum allowable measurement noise that can be experienced by the vision-based navigation system to achieve mission success.

The M-SAT team is also limited by the propellant type and usage. The M-SAT team requires that the propellant used be non-volatile, non-combustable, inexpensive, and efficient. A trade study at Missouri S&T was accomplished by Seubert[29] that concluded that R-134a would be a suitable propellant compared to other cold-gas propulsion options. R-134a is a common automotive refrigerant that is inexpensive and easily obtainable. At twenty degrees Celsius, R-134a reaches a saturation pressure below the AFRL mandated pressure requirement. This allows R-134a to be stored as a saturated liquid and expelled as a gas. At a tank volume of 2600 cubic centimeters and a pressure of 689.5 kPa, 2.3 kg of propellant can be stored. This translates to a net velocity change budget of 20.0 meters per second (assuming a MR SAT wet mass of 25 kg).

2.2.3. Satellite Configuration. The M-SAT spacecraft are configured as a small satellite stack. MR SAT and MRS SAT are mated at launch. After launch vehicle ejection and an initial detumble phase, the spacecraft are separated with a release mechanism that imparts, theoretically, no relative separation velocity between the spacecraft. To conserve propellant, this release mechanism is augmented with a series of springs to provide a low net ejection velocity to the satellite pair. The springs impart a relative separation velocity to the spacecraft which places MR SAT on an invariant manifold that transfers MR SAT

to the desired true anomaly separated formation position. MR SAT and MRS SAT are launched in a mated configuration. Figure **2.1** shows the satellite stack in mated configuration.

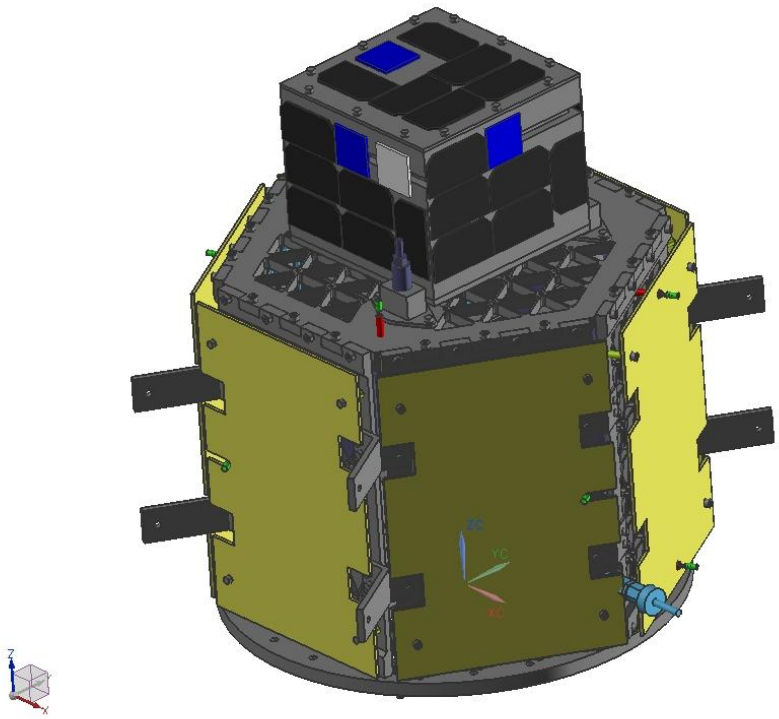

Figure 2.1. Mated Satellite Configuration

MR SAT is a hexagonal prism made of isogrid aluminum 6061 panels. The spacecraft is electrically powered by 90 high efficiency solar cells. A series of twelve thrusters is utilized to provide six degree-of-freedom control to the spacecraft in order to perform attitude and orbit control simultaneously.

MRS SAT is the smaller of the two spacecraft. It is a cubical structure that relays recorded GPS data to MR SAT via a wireless connection for data verification during post processing. It is noted that the autonomous control is based upon the visual navigation

system, and not the relayed GPS data. Table 2.3 shows the specific parameters for MR SAT and MRS SAT utilized in the simulations.

Table 2.3: Spacecraft Physical Properties

	MR SAT	MRS SAT
Mass (kg)	24.82	15.71
Volume (cm x cm x cm)	33 x 33 x 45	10 x 10 x 10
Cross Sectional Area (m^2)	0.286	0.143
Coefficient of Drag	1.0	1.0
Ballistic Coefficient (kg/m^2)	86.69	109.86

The thrusters have undergone a series of tests at Missouri S&T. Pahl[30] et al. have determined that each thruster can produce twenty-four millinewtons of thrust when open and operating in a vacuum with a back pressure of 165.5 kPa. The control saturation thrust level is defined as forty-eight millinewtons in every direction. This assumes that an attitude control system is able to rotate the MR SAT spacecraft to an orientation where two thrusters are pointing in the desired thrust direction.

The data path for the control and state estimation software utilized on board MR SAT is critical for correct modeling of the system architecture and key to designing navigation paths and control systems. All data processing during the M-SAT mission is done autonomously on board MR SAT. Figure 2.2 shows the data path for the satellite pair. The MR SAT position and velocity are measured at a rate of one hertz from a GPS receiver on board MR SAT. The raw GPS measurements are then filtered using an Unscented Kalman Filter (UKF) to formulate a state estimate for MR SAT. The MRS SAT states are measured from some vision based navigation system. The vision based navigation system is assumed to provide position and velocity of MRS SAT in the Earth Centered Earth Fixed (ECEF) inertial frame.

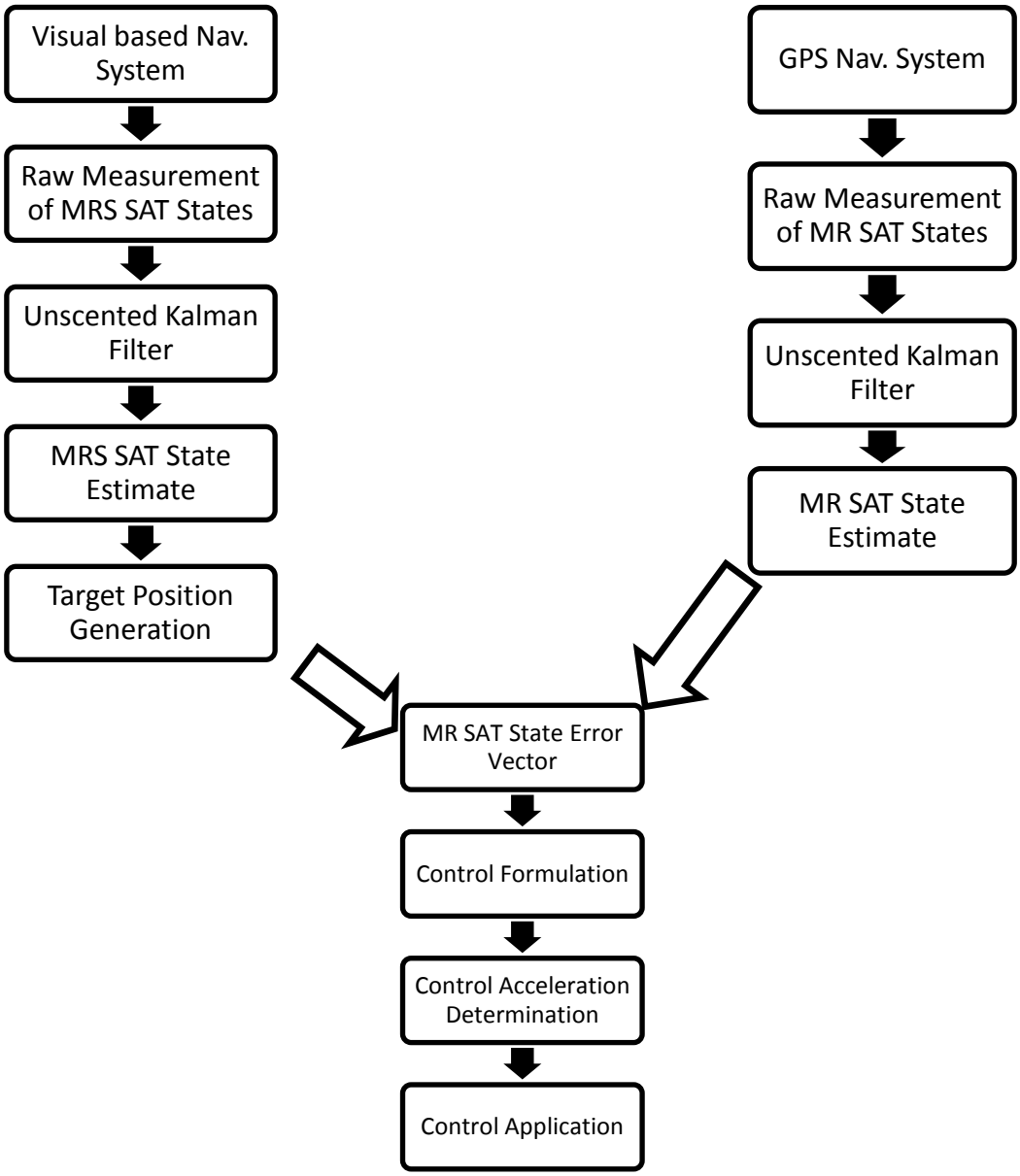

Figure 2.2. M-SAT Mission Data Path

The raw measurements for MRS SAT is then filtered by a UKF to formulate a state estimate for MRS SAT. The target position for MR SAT is then populated from the MRS SAT state estimate. A state error vector is defined as the difference between the

MR SAT state estimate and the target position. The control acceleration is defined as the multiplication of the control gain and the state error vector. Finally, the control acceleration is applied via the cold gas propulsion system on board MR SAT. This process is repeated at each time step during the simulation.

3. SIMULATION PARAMETERS

3.1. SATELLITE INITIAL CONDITIONS

The Nanosat competition provides a launch to an initial LEO orbit in the 300-1000 km altitude range with near zero eccentricity. To enhance the atmospheric drag perturbations on both spacecraft during simulations, the altitude is selected to be 300 km. The initial orbital eccentricity is defined to be a near zero value. Other orbit parameters are dependent upon the specific launch opportunity and are therefore defined as zero for this study. The spacecraft's position is initialized in a low Earth orbit with the classical orbital elements

$$[a \quad e \quad i \quad \Omega \quad \omega \quad v] = [6678.145\,\text{km} \quad 0.01 \quad 0 \quad 0 \quad 0 \quad 0] \tag{1}$$

This provides an initial scenario where the spacecraft are separated at the ascending node and at periapsis.

3.2. MISSION TIMELINE

MR SAT and MRS SAT are initially mated at launch. The satellite stack is then ejected after launch vehicle burnout. MR SAT employs a series of magnetic torque coils to mitigate and eventually eliminate tip off error caused by the satellite-launch vehicle separation mechanism. The satellite pair will then proceed with a series of systems checks and operational verification routines. Upon approval from the ground the satellite pair will separate and MR SAT will drift to a pre-defined true anomaly separated formation. Figure 3.1 shows the separation at perigee, an along-track drift to the separation point, and formation stabilization at a fixed distance, *R*. The choice to separate the spacecraft at perigee is arbitrary and does not affect the local system dynamics for a near circular orbit. The distances in Figure 3.1 are not to scale and meant for illustrative purposes only.

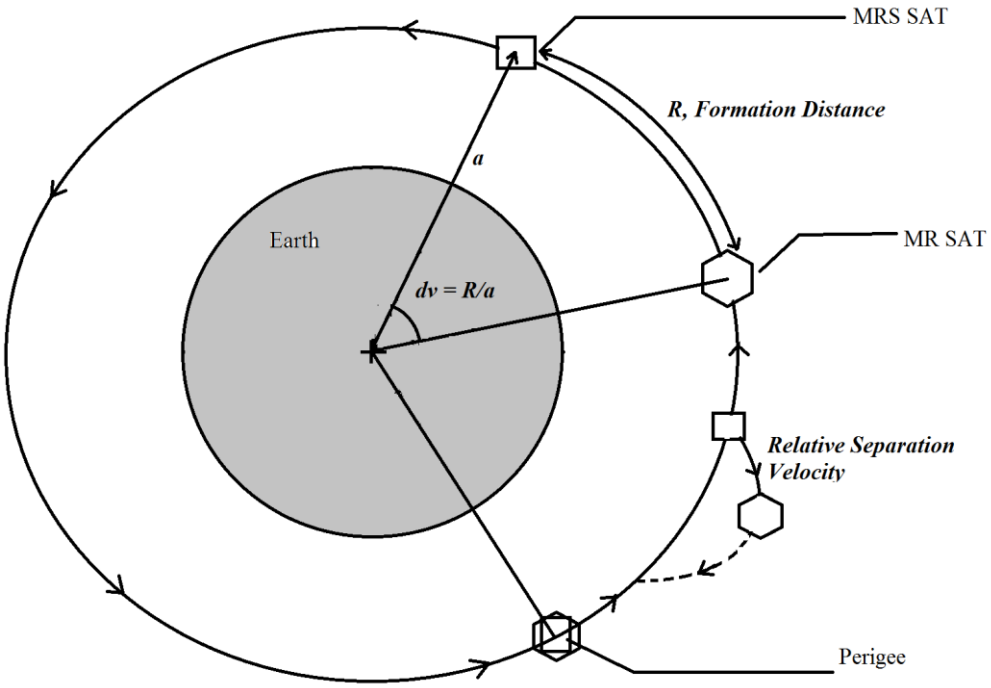

Figure 3.1. Spacecraft Separation, Drift, and Formation Stabilization

After performing station keeping for half an orbit, MR SAT will initiate a circumnavigation maneuver. MR SAT will continue along this path until a fuel limitation is reached and then will return to the initial true anomaly separated formation until the fuel supply is depleted. MR SAT will then perform extended mission operations involving a Bluetooth range test and eventual reentry. This study investigates the spacecraft separation, true anomaly separated formation, and a single circumnavigation.

3.3. SATELLITE SEPARATION

The satellite separation phase consists of MR SAT ejecting MRS SAT and drifting to the true anomaly separated formation. The ejection direction can be calculated as a function of ejection velocity and true anomaly separation angle, and is slightly out of the in-track-radial plane in the LVLH frame in order to place MR SAT on an invariant manifold to the desired location. After detachment the thrusters will not fire and MR SAT will drift back to the desired distance. MR SAT will then activate the propulsion system.

Previous work by the author utilized a Monte-Carlo approach to determine a fuel efficient location to initiate the active control for a given ejection velocity. The ejection velocity, arbitrarily chosen for this study, is 0.05 meters per second and the corresponding control-on location is two meters from the target true anomaly separation location for a true anomaly separation arc length of twenty five meters. Future work could focus on optimizing these parameters to increase fuel efficiency of the mission.

The separation direction is purely in the radial and along track frame. Future work could incorporate the cross track motion, however for simplicity can be ignored because the cross track motion decouples in the local linearized dynamic model.

3.4. TRUE ANOMALY SEPARATED FORMATION

MR SAT assumes an initial formation to stabilize the relative motion between the spacecraft and then executes a series of initial operational tests before performing the circumnavigation.

The true anomaly separation is chosen due to the relative motion mitigation that occurs for small formation sizes. Earth oblateness and third-body effects on the relative motion are assumed to be negligible due to the small formation size relative to the radial distance and the third-body distances. Solar radiation pressure is also assumed to be negligible and not included in the dynamic model. Atmospheric drag in a true anomaly separated formation is a perturbation (also referred to as “differential drag”) that may alter the satellites’ relative motion in a significant way. The amount of relative motion change is dependent on several factors, most significantly eccentricity, semimajor axis, and ballistic coefficient. The semimajor axis and eccentricity are similar during a true anomaly separated formation, thus the ballistic coefficient differential is a factor which contributes to the instability of the true anomaly separated formation.

The MR SAT target location is determined by taking the available Cartesian position and velocity of MRS SAT as given by the on-board GPS receiver, filtering the data, obtaining the classical orbital elements, subtracting an arc length from the true anomaly, and transforming the resulting orbital elements to Cartesian form for use in the control algorithms. The target true anomaly for MR SAT is given by

$$\nu_{MR\ SAT} = \nu_{MRS\ SAT} - R/a_{MRS\ SAT} \tag{2}$$

where R = formation separation distance.

Then the conversion from classical elements to Cartesian form proceeds as

$$\begin{Bmatrix} a_{Target} \\ e_{Target} \\ i_{Target} \\ \Omega_{Target} \\ \omega_{Target} \\ \nu_{Target} \end{Bmatrix}_{MR\ SAT} = \begin{bmatrix} a_{MRS\ SAT} \\ e_{MRS\ SAT} \\ i_{MRS\ SAT} \\ \Omega_{MRS\ SAT} \\ \omega_{MRS\ SAT} \\ \nu_{MRS\ SAT} \end{bmatrix} - \begin{bmatrix} 0 \\ 0 \\ 0 \\ 0 \\ 0 \\ \nu_{MR\ SAT} \end{bmatrix} \tag{3}$$

$$\begin{Bmatrix} x_{Target} \\ y_{Target} \\ z_{Target} \\ \dot{x}_{Target} \\ \dot{y}_{Target} \\ \dot{z}_{Target} \end{Bmatrix} = [DCM] \begin{Bmatrix} r \\ 0 \\ 0 \\ V_x \\ V_y \\ V_z \end{Bmatrix} \tag{4}$$

where $r = \frac{h^2}{\mu_E}(1 + e\cos\nu)^{-1}$,

$$\begin{Bmatrix} V_x \\ V_y \\ V_z \end{Bmatrix} = \begin{bmatrix} \mu_E e \sin\nu/h \\ h/r \\ 0 \end{bmatrix},$$

and $h = \sqrt{\mu_E a(1 - e^2)}$

MR SAT is commanded to hold this position for half an orbital period. This initial holding position is chosen as an operational checkout point to ensure that all systems are functioning properly.

3.5. INSPECTION PATH DESIGN

Upon completion of the station keeping and formation stabilization maneuver, MR SAT autonomously begins circumnavigation of MRS SAT. A periodic solution to the Hill [3] equations exists that provides a control free path about the origin in the LVLH frame. This section shows the derivation of that natural solution and the assumptions made to apply the solution to the M-SAT mission, starting with the Hill equations

$$\begin{aligned} \ddot{x} - 2\dot{y} - 3x &= 0 \\ \ddot{y} + 2x &= 0 \\ \ddot{z} + z &= 0 \end{aligned} \tag{5}$$

A natural periodic solution is desired to these linearized set of equations. In the subsequent derivations, $\hat{x}$ lies in the radial direction away from the Earth, $\hat{y}$ lies in the direction of the local horizon, and $\hat{z}$ lies normal to the orbit plane in the direction of angular momentum.

Note that the motion in the z direction decouples, which is convenient for solving the second order non-homogenous differential equations. The general solution may be obtained as

$$\begin{aligned} x(\tau) &= a_1 + a_3 \cos\tau + a_4 \sin\tau \\ y(\tau) &= a_2 + \frac{3}{2} a_1 \tau + 2a_4 \cos\tau - 2a_3 \sin\tau \\ z(\tau) &= a_5 \cos\tau + a_6 \sin\tau \end{aligned} \tag{6}$$

To ensure bounded stable motion about MRS SAT (which is placed at the origin), it is convenient to eliminate the secular terms that may cause the relative motion to grow unbounded as time approaches infinity by setting $a_1 = a_2 = 0$.

It is then possible to find the remaining constants by differentiating Equation 6 twice and using the original Hill equations, resulting in

$$\begin{gathered}\ddot{x}(\tau) = -a_3 \cos\tau - a_4 \sin\tau \rightarrow \ddot{x}(0) = -a_3 = \dot{y}_0 + 3x_0 \rightarrow a_3 = -\dot{y}_0 - 3x_0 \\ \ddot{y}(\tau) = -2a_4 \cos\tau + 2a_3 \sin\tau \rightarrow \ddot{y}(0) = -2a_4 = -2\dot{x}_0 \rightarrow a_4 = \dot{x}_0 \\ \ddot{z}(\tau) = -a_5 \cos\tau - a_6 \sin\tau \rightarrow \ddot{z}(0) = -a_5 = -z_0\end{gathered} \tag{7}$$

The solution for a_6 is found by differentiating the cross-track differential equation once, giving

$$\dot{z}(\tau) = -a_5 \sin\tau + a_6 \cos\tau \rightarrow \dot{z}(0) = a_6 = \dot{z}_0 \tag{8}$$

Because it is desirable to be able to pick a circumnavigation distance and produce a periodic solution from that single piece of information, it is desirable to write the equations of motion in phase/amplitude form as

$$\begin{gathered}x(\tau) = -A\cos(\tau + \phi) \\ y(\tau) = 2A\sin(\tau + \phi) \\ z(\tau) = B\sin(\tau + \psi)\end{gathered} \tag{9}$$

It is desired that the solution begin in the along-track direction at a distance equivalent to the true anomaly separated formation size. Utilizing this initial condition, it is possible to obtain the amplitude A as

$$y(0) = -R = 2A \rightarrow A = -\frac{R}{2} \tag{10}$$

Another useful relationship that is exploitable is the desire to have a fixed circumnavigation distance, which is useful for determining the amplitude B using

$$\begin{aligned} R &= \sqrt{x(\tau)^2 + y(\tau)^2 + z(\tau)^2} \\ &= \sqrt{\frac{R^2}{4} cos^2(\tau + \phi) + R^2\, sin^2(\tau + \phi) + B^2\, sin^2(\tau + \psi)} \end{aligned} \tag{11}$$

Solving equation 11 for the amplitude B gives

$$B = \frac{\sqrt{3} R\, cos(\tau + \phi)}{2\, sin(\tau + \psi)} \tag{12}$$

The phase/amplitude form of the circumnavigation path then becomes

$$\begin{aligned} x(\tau) &= -\frac{R}{2} cos(\tau + \phi) \\ y(\tau) &= R\, sin(\tau + \phi) \\ z(\tau) &= \frac{\sqrt{3} R}{2} cos(\tau + \phi) \end{aligned} \tag{13}$$

Notice that the cross-track motion phase angle is cancelled when substituting Equation 12 into Equation 9. This is due to the selection of the initial conditions for finding the

amplitude A. Since the along-track starting position is selected, it is possible to alter the phase angle to select a positive or negative along-track starting location. A negative along-track starting location can be selected using

$$y(0) = R\,sin(\phi) = -R \rightarrow \phi = sin^{-1}(-1) = \frac{3\pi}{2} \tag{14}$$

The target path definition equations for a fixed distance circumnavigation about a target starting from a negative along-track position is then given by

$$\begin{aligned} x(\tau) &= -\frac{R}{2} cos\left(\tau + \frac{3\pi}{2}\right) \\ y(\tau) &= R\,sin\left(\tau + \frac{3\pi}{2}\right) \\ z(\tau) &= \frac{\sqrt{3}R}{2} cos\left(\tau + \frac{3\pi}{2}\right) \end{aligned} \tag{15}$$

In order to make this method practical, it is desired to define the angle τ, the segmentation angle factor, at each point during the simulation as

$$\tau_i = \frac{2\pi t_i}{\left(2\pi\sqrt{\frac{a^3}{\mu_E}}\right)} = \frac{t_i}{\left(\sqrt{\frac{a^3}{\mu_E}}\right)} \tag{16}$$

where t_i is the time since the maneuver initiation time, a is the semimajor axis of the RSO, and μ_E is the gravitational parameter of Earth. Notice that the denominator of

Equation 16 is equivalent to the MRS SAT orbital period. This is because the closed form solution to the Hill equations is periodic over one orbital period.

The inspection ring is divided into a set of discrete points based upon the total length and time step of the simulation. Each time step is then associated with a ring arc segment and the inspector satellite is commanded to follow each arc sequentially.

3.6. DYNAMIC MODEL

The system state variables are propagated using a model incorporating Earth oblateness, third-body lunar and solar effects, and atmospheric drag. The system dynamic model in state factored state space form is defined by

$$\begin{Bmatrix} \dot{x} \\ \dot{y} \\ \dot{z} \\ \ddot{x} \\ \ddot{y} \\ \ddot{z} \end{Bmatrix} = \begin{bmatrix} 0 & 0 & 0 & 1 & 0 & 0 \\ 0 & 0 & 0 & 0 & 1 & 0 \\ 0 & 0 & 0 & 0 & 0 & 1 \\ -\frac{\mu_E}{\Lambda^3}(k_1 + k_2 R_\Phi) - k_3 R_w & -\frac{\mu_E}{\Lambda^3} k_2 R_\Phi - k_3 R_w & -\frac{\mu_E}{\Lambda^3} k_2 R_\Phi - k_3 R_w & k_3 & 0 & 0 \\ -\frac{\mu_E}{\Lambda^3} k_2 R_\Phi - k_3 R_w & -\frac{\mu_E}{\Lambda^3}(k_1 + k_2 R_\Phi) - k_3 R_w & -\frac{\mu_E}{\Lambda^3} k_2 R_\Phi - k_3 R_w & 0 & k_3 & 0 \\ -\frac{\mu_E}{\Lambda^3} k_2 R_\Phi - k_3 R_w & -\frac{\mu_E}{\Lambda^3} k_2 R_\Phi - k_3 R_w & -\frac{\mu_E}{\Lambda^3}(k_1 + k_2 R_\Phi) - k_3 R_w & 0 & 0 & k_3 \end{bmatrix} \begin{Bmatrix} x \\ y \\ z \\ \dot{x} \\ \dot{y} \\ \dot{z} \end{Bmatrix} + \begin{bmatrix} 0 & 0 & 0 \\ 0 & 0 & 0 \\ 0 & 0 & 0 \\ 1 & 0 & 0 \\ 0 & 1 & 0 \\ 0 & 0 & 1 \end{bmatrix} \begin{Bmatrix} u_x \\ u_y \\ u_z \end{Bmatrix} \tag{17}$$

where $k_1 = 1 - \frac{3J_2}{2}\left(\frac{R_E}{\Lambda}\right)^2 (3\sin^2(L) - 1) + \frac{\mu_S}{\mu_E}\left(\frac{\Lambda}{R_S}\right)^3 + \frac{\mu_M}{\mu_E}\left(\frac{\Lambda}{R_M}\right)^3,$ (18)

$$k_2 = \frac{3J_2}{\Lambda}\left(\frac{R_E}{\Lambda}\right)^2 \sin L, \tag{19}$$

$$k_3 = -\frac{V_{rel}}{2\beta}\rho_0 e^{-\frac{\Lambda}{H}}, \tag{20}$$

and $\Lambda = \left\| \begin{Bmatrix} x \\ y \\ z \end{Bmatrix} \right\|$ (21)

The dynamic system is propagated using a fixed step size Runge-Kutta 4th order integration. This scheme is chosen due to its accuracy and implicit nature. Because the propagation time is small and the initial conditions are reset at each time step, a higher

order integrator was deemed unnecessary for this thesis. A more detailed and high fidelity model may be used in the future when an initial orbit range is better defined as a way to provide a more accurate representation of the system. The time steps for the simulation are chosen as one second. Future work could involve varying this simulation time step to improve performance.

3.7. CONTROLLER DESIGN

A linear quadratic regulator is selected as the controller to provide the satellite command acceleration. Previous work by the author has suggested that for small (less than fifty meter arc length) true anomaly separated formations using small spacecraft, a linear controller based upon a factorized nonlinear dynamic model provides similar control commands and efficiencies when compared to a nonlinear controller. However, because circumnavigation involves possible additional nonlinear factors, it was decided that that a controller comparison be made between a linear and a nonlinear controller.

It should be noted that in order to limit chattering and excessive fuel usage about the target solution, all control command accelerations when the spacecraft is within one meter (root mean square) of the target location are set to zero. This distance is arbitrarily chosen and not optimized in any way. Future work intends to optimize this distance as a means of improving performance.

3.7.1. LQR Controller. The infinite-horizon, continuous-time linear quadratic regulator (LQR) controller is a state feedback control law that minimizes the value of the associated quadratic cost function. For this specific simulation, GPS receivers, or some other orbit determination hardware, provide approximations for each state and the LQR controller utilizes this information to calculate a control gain. This specific controller utilizes dynamics given by the model in Equation 17 as the plant matrix. Future plans are to incorporate a simpler HCW-based model for the controller, however, this study uses the same model to propagate the system dynamics and produce the control output. A general cost function is defined as

$$J = \frac{1}{2}\int_0^\infty \{x^T Q x + u^T R u\}\, dt \tag{22}$$

where the weight associated with state errors Q is and the control weight R are given by

$$Q = diag([1 \quad 1 \quad 1 \quad 1 \quad 1 \quad 1] \tag{23}$$

$$R = diag\left(\left[\left(\frac{\mu_E}{\|x_{tgt}\|^3}\right)^{-1} \quad \left(\frac{\mu_E}{\|x_{tgt}\|^3}\right)^{-1} \quad \left(\frac{\mu_E}{\|x_{tgt}\|^3}\right)^{-1}\right]\right)$$

The controller weights are based off of previous work on the CanX 4&5 FIONA controller[10]. Future work intends to use an LQR tuning algorithm to achieve better system performance for this specific application. The resulting algebraic Riccati equation and control gain calculation are

$$A^T P + PA - PBR^{-1}B^T P + Q = 0 \tag{24}$$

$$K = R^{-1}B^T P \tag{25}$$

Using the controller gain, the control law that minimizes the cost function can be calculated as

$$u = -Ke \tag{26}$$

$$\text{where } e = \begin{bmatrix} x_{tgt} - x_{INSPECTOR} \\ v_{tgt} - v_{INSPECTOR} \end{bmatrix}$$

The LQR controller attempts to drive the error between the position and the velocity to zero. However it does so in a way that minimizes the overall cost function. The controller gain for the LQR control scheme, K, is only calculated at the first time step during the simulation. In the true anomaly separated formation, the error vector consists of both the position and velocity error. In order to keep the analysis conservative, only the position error was used in the circumnavigation portion of the simulation. Future work intends to differentiate Equation 15 to achieve a target position for use in the state error vector.

3.7.2. SDRE Controller. The SDRE controller is derived in the same way, however, it evaluates the gain, $\boldsymbol{K}$, at each time step. This utilizes the solution to the state dependant Riccati equation. Future efforts will compare this controller algorithm to other controller formulations, specifically sliding mode and neural network control.

3.8. STATE ESTIMATION

The Unscented Kalman Filter (UKF) was first derived by Julier and Uhlmann[33] in 1997 as a method to eliminate the inefficiencies that the Extend Kalman Filter (EKF) possessed. A UKF is used to estimate the noisy states for MR SAT and MRS SAT. It is chosen because, contrary to an Extended Kalman Filter, propagation of the covariance matrix is not achieved through linearization of the nonlinear dynamic model. The UKF is based off the deterministic sampling of a set of sigma points that are propagated using the nonlinear dynamics. A weighted average of the propagated sigma points is taken to recover the state estimate and the covariance. The UKF is formulated by choosing a set of sigma points as

$$\hat{x}_k^i = f\left(\hat{x}_{k-1}^+ + \tilde{x}^i\right) + \boldsymbol{Bu} \tag{27}$$

$$\text{where } \tilde{\mathrm{x}}^{\mathrm{i}} = \left(\sqrt{\mathrm{nP}_{\mathrm{k-1}}^{+}}\right)_{\mathrm{i}}^{\mathrm{T}} \qquad \mathrm{i} = 1,2,\dots,\mathrm{n}$$

$$\text{and where } \tilde{x}^{i+n} = -\left(\sqrt{nP_{k-1}^+}\right)_i^T \qquad i = 1,2,\dots,n$$

where n is the size of the state vector, i designates the i^{th} column of the resulting square root matrix, $P_{k-1}^+$is the *a posteriori* covariance matrix from the previous time step, $\hat{x}_{k-1}^+$ is the *a posteriori* state estimate from the previous time step, and $\boldsymbol{u}$ is the three dimensional acceleration vector calculated by the control algorithm. Due to the

inaccuracies inherent in taking the numerical square root of a matrix, Cholesky decomposition is used to provide a matrix S such that $SS^T = nP_{k-1}^+$. The sigma points, $\hat{x}_k^i$, are then summed and weighted to provide an average state estimate using

$$\hat{x}_k^- = \frac{1}{2n}\sum_{i=1}^{2n}\hat{x}_k^i \tag{28}$$

The process of calculating an *a priori* covariance and measurement estimate from the *a priori* state estimate and sigma points is shown by

$$P_k^- = \frac{1}{2n}\sum_{i=1}^{2n}\left(\hat{x}_k^i - \hat{x}_k^-\right)\left(\hat{x}_k^i - \hat{x}_k^-\right)^T + Q_k \tag{29}$$

$$\hat{y}_k = \frac{1}{2n}\sum_{i=1}^{2n} h\left(\hat{x}_k^i\right) \text{ where } h = 1 \tag{30}$$

The Kalman gain can be calculated using

$$K_k = P_{xy}{P_y}^{-1} \tag{31}$$

where $P_{xy} = \frac{1}{2n}\sum_{i=1}^{2n}\left(\hat{x}_k^i - \hat{x}_k^-\right)\left(\hat{y}_k^i - \hat{y}_k\right)^T$,

and $P_y = \frac{1}{2n}\sum_{i=1}^{2n}\left(\hat{y}_k^i - \hat{y}_k\right)\left(\hat{y}_k^i - \hat{y}_k\right)^T + \mathrm{R}$

The *a posteriori* state estimate and the *a posteriori* covariance are formulated as

$$\hat{x}_k^+ = \hat{x}_k^- + K_k(y_k - \hat{y}_k) \tag{32}$$

$$P_k^+ = P_k^- - K_k P_y {K_k}^T \tag{33}$$

The above steps are completed at each time step using Runge-Kutta 4th order integration to propagate the sigma points to the next time step. The initial covariance for the states of both spacecraft was chosen as

$$P_o = diag([5 \times 10^4 \quad 5 \times 10^4 \quad 5 \times 10^4 \quad 1 \times 10^2 \quad 1 \times 10^2 \quad 1 \times 10^2]) \tag{34}$$

This value was arbitrarily chosen because MR SAT will begin estimating the states well before the satellite separation and the initial covariance choice should therefore not influence the steady state errors. In order to present a conservative analysis, it is assumed that the state estimation begins at satellite separation; however, as is seen in the results, the effects of the initial covariance errors are mitigated as the time duration of the simulation increases.

4. NUMERICAL RESULTS AND ANALYSIS

4.1. INITIAL RESULTS

The circumnavigation ring orientation is defined such that the motion of the inspector spacecraft is along the invariant manifold predicted by the Hill equations. The target path for MR SAT is shown below for the circumnavigation stage of the mission. The total time span for these simulations is equivalent to 1.5 orbital periods of MRS SAT. Figure 4.1 shows the MR SAT target path. Note that MRS SAT is fixed at the origin.

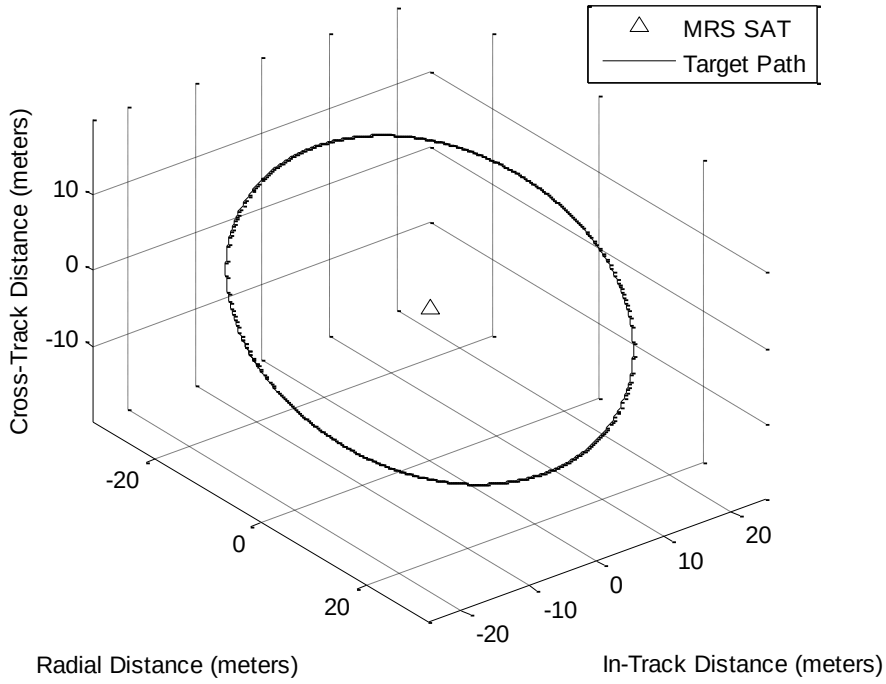

Figure 4.1. Circumnavigation Path

MR SAT is initialized in a mated configuration at the origin. MR SAT is then commanded to separate and drift to a true anomaly separation formation and hold that

position. The true anomaly separation arc length, R, is arbitrarily chosen as twenty-five meters. After an arbitrarily chosen time duration (half an orbital period), MR SAT is commanded to follow the circumnavigation ring, starting in the positive cross track direction and eventually returning to the original holding position.

A controller comparison is important in order to obtain an understanding of the dynamic system and the control accuracy required to perform the M-SAT mission. These simulations are run with zero measurement and zero state process noise.

4.2. CONTROLLER COMPARISON

A comparison between linear and nonlinear control schemes is outlined in the section below. Comparing a linear quadratic regulator to an SDRE controller is aimed at developing effective on-orbit autonomous control laws and flight computer CPU requirements.

The error from the target path is important in assessing controller performance and the ability of a controller to track the desired inspection path. Figure 4.2 shows the path taken by the LQR and SDRE control algorithms under the same initial conditions given in Equation 1 (the simulation begins at spacecraft separation).

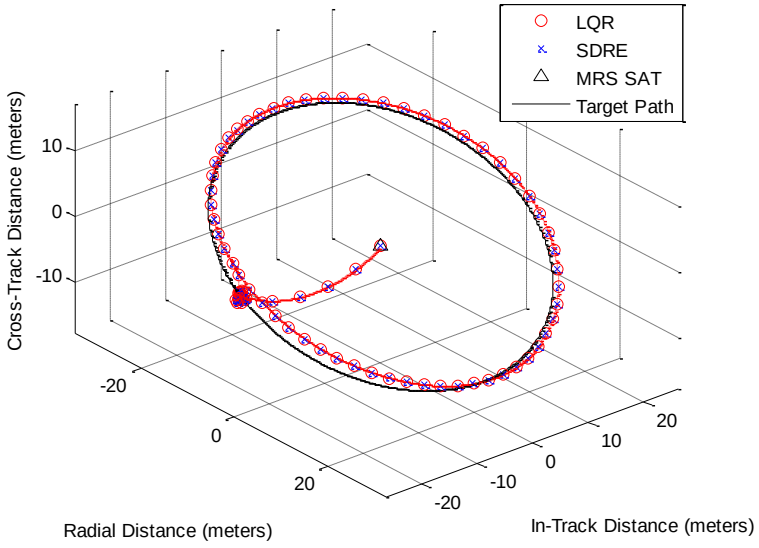

Figure 4.2. LQR and SDRE Tracked Path

Both the LQR and SDRE controller track the desired inspection path similarly at this formation size. Figure 4.3 shows the root mean square deviation from the desired path of MR SAT.

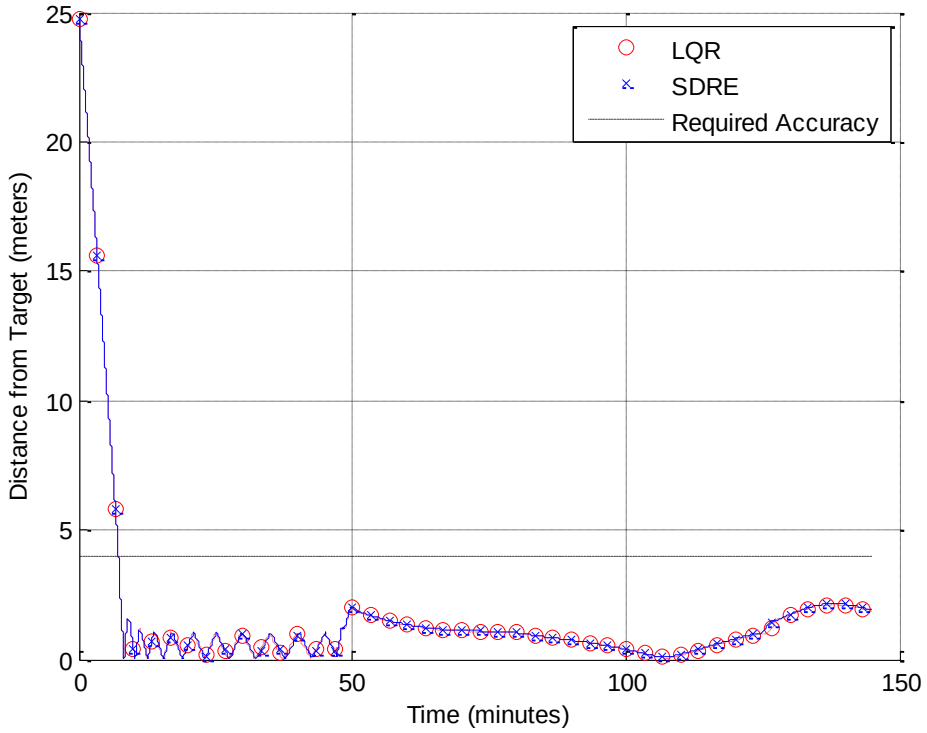

Figure 4.3. LQR and SDRE RMS Position Error

The oscillations about the target position are caused by the deadband imposed on the control algorithm. It can be seen that both controllers track the solution in a similar way. The maximum deviation from the target path, after it is first reached, is less than four meters which satisfies the requirement given by the M-SAT mission requirements.

Figure 4.4 shows the tracking for the LQR and SDRE controllers along the three principle axes.

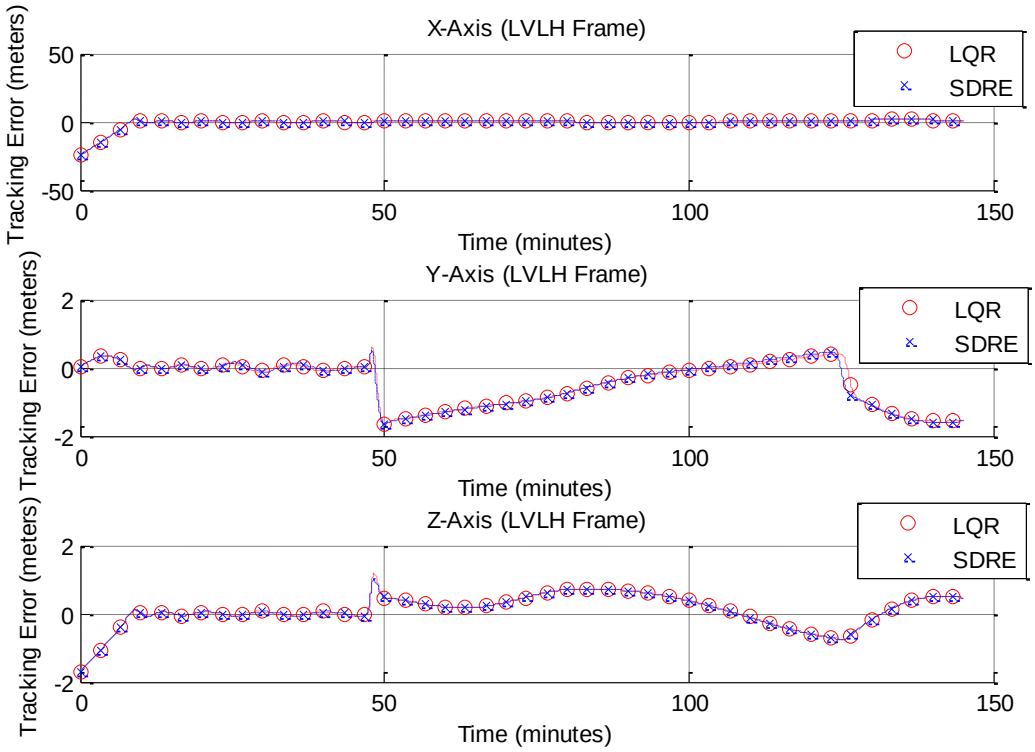

Figure 4.4. Tracking Error Along the Three Principal Axes

The LQR and SDRE controller track the solution similarly along each of the three axes. The tracking solution oscillates about an error value of zero. This emphasizes the similarity between the linear and nonlinear control efficiencies for this specific system and set of initial conditions.

The velocity change experienced during the simulated mission is shown in Figure 4.5. The velocity change is significantly less than the twenty meters per second budget available for the M-SAT mission. This initial result implies that the MR SAT can perform multiple circumnavigations to better accomplish the mission objectives. The initial results also show that the M-SAT mission can be accomplished using this hardware arrangement (noting that zero system noise has been assumed).

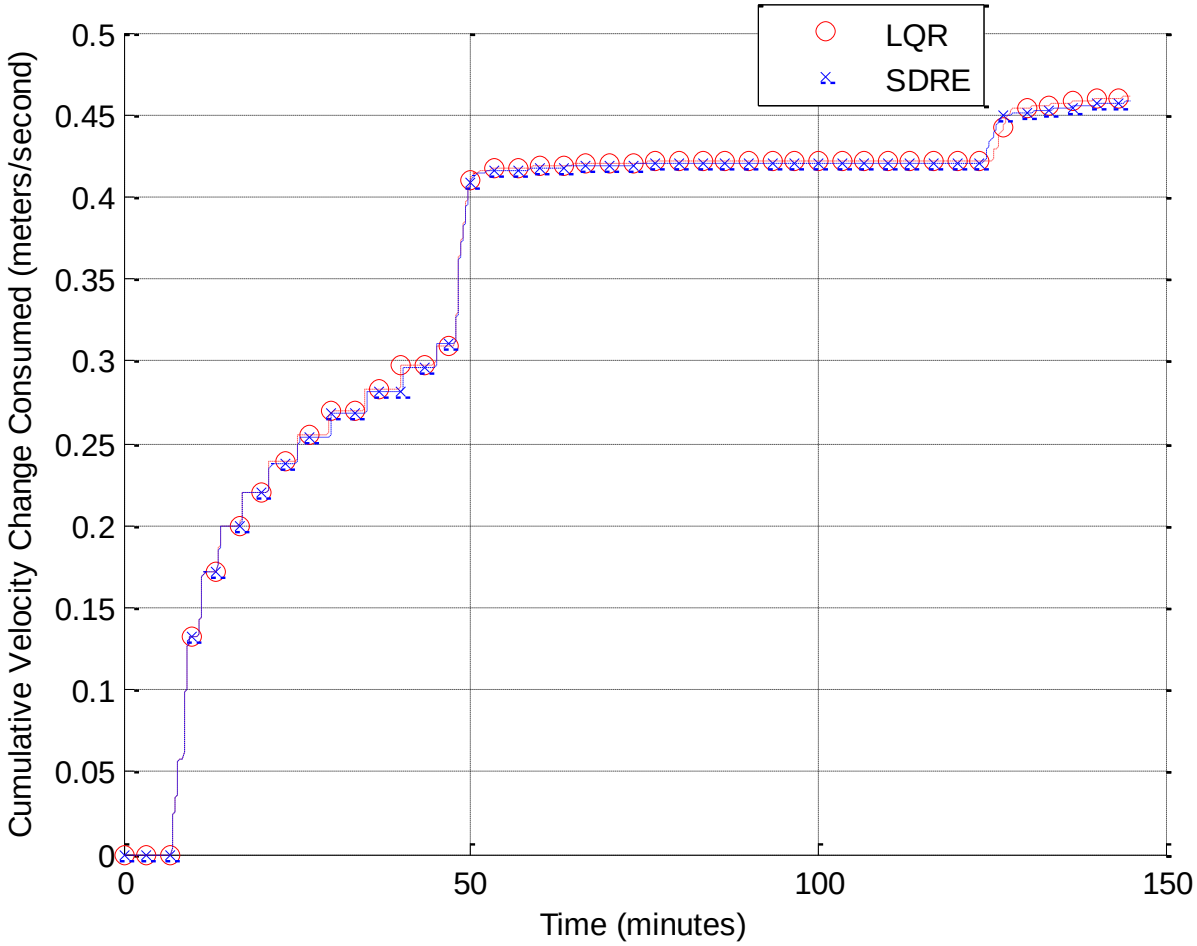

Figure 4.5. LQR and SDRE Cumulative Velocity Change

Control saturation is one key factor in determining the efficacy of a control algorithm. The control saturation limit was set at 48 millinewtons, twice the theoretical thrust maximum of each thruster on MR SAT. To observe if control saturation is occurring, the commanded control is plotted in Figure 4.6.

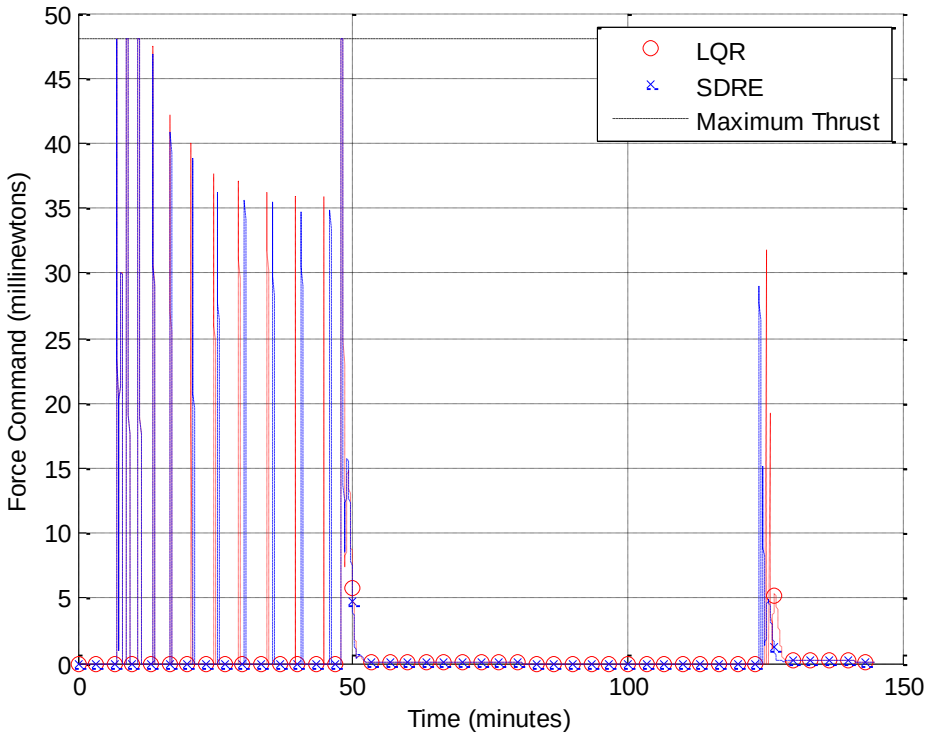

Figure 4.6. Command Control Saturation

The LQR and SDRE controllers saturate the thrust system four times during the simulation. The main thrust pattern is in the form of short bursts during the true anomaly separated formation to station keep at a fixed distance. This is caused by the deadband imposed on the spacecraft control algorithm. The fourth, and last, saturation occurs when the circumnavigation maneuver is initiated. Once the invariant manifold path is achieved, however, the control input is minimized until perturbations drive the spacecraft away

from the target path by more than one meter. This deviation causes the spacecraft to utilize the propulsion system to reestablish the target path.

4.3. MEASUREMENT NOISE EFFECTS

Visual-based navigation provides a less precise measurement of a target spacecraft than relayed GPS data. The goal of the set of simulations described in this section is to assess how imprecise state estimates can compromise mission requirements. The analysis procedure is to increase the measurement noise addition to the MRS SAT state, filter the MRS SAT data using an Unscented Kalman Filter, and use the estimated states to perform the nominal circumnavigation. The MR SAT measurement data are also corrupted with white Gaussian noise to simulate measurement noise from GPS measurements. The GPS units have been sourced as NovaTel OEMV-1 GPS units. Therefore, the MR SAT measurement noise is assumed as the manufacturer specified measurement noise data and is held constant through all simulations. State process noise is also included as Gaussian white process noise. Table 4.1 shows the white noise which is added to the measurement data prior to filtering.

Table 4.1. Measurement Noise Addition

	MR SAT	**MRS SAT**
Measurement Noise $[x \quad y \quad z \quad \dot{x} \quad \dot{y} \quad \dot{z}]$ (meters and meters/second)	2.2 $* Diag([1 \quad 1 \quad 1 \quad 0.1 \quad 0.1 \quad 0.1])$	n $* Diag([1 \quad 1 \quad 1 \quad 0.1 \quad 0.1 \quad 0.1])$ where n is an integer which varies between simulations
State Process Noise $[x \quad y \quad z \quad \dot{x} \quad \dot{y} \quad \dot{z}]$ (meters and meters/second)	$Diag([1 \quad 1 \quad 1 \quad 0.1 \quad 0.1 \quad 0.1])$	$Diag([1 \quad 1 \quad 1 \quad 0.1 \quad 0.1 \quad 0.1])$

The effect of the measurement noise is evaluated against the mission requirements. The measurement noise factor on the simulated measurement of the MRS SAT states is increased and the resulting target path deviations and velocity change is plotted to determine the maximum Gaussian white noise standard deviation that is acceptable for the M-SAT mission. These data will eventually be utilized in the process to select and procure flight hardware.

The LQR and SDRE controllers are also compared during the noisy scenarios to assess the effects of noise on controller performance.

4.3.1. Probable Measurement Noise Scenario. A preliminary investigation into candidate visual-based navigation systems has led to a suggested measurement noise level for such systems. This scenario is run as a case study and with a value of $\boldsymbol{n = 5}$. The root mean square difference between the UKF estimated position and the true position for MR SAT using the LQR control scheme, MR SAT using the SDRE control scheme, and MRS SAT are plotted versus time in Figure 4.7. Note that this should not be confused with guidance path tracking error.

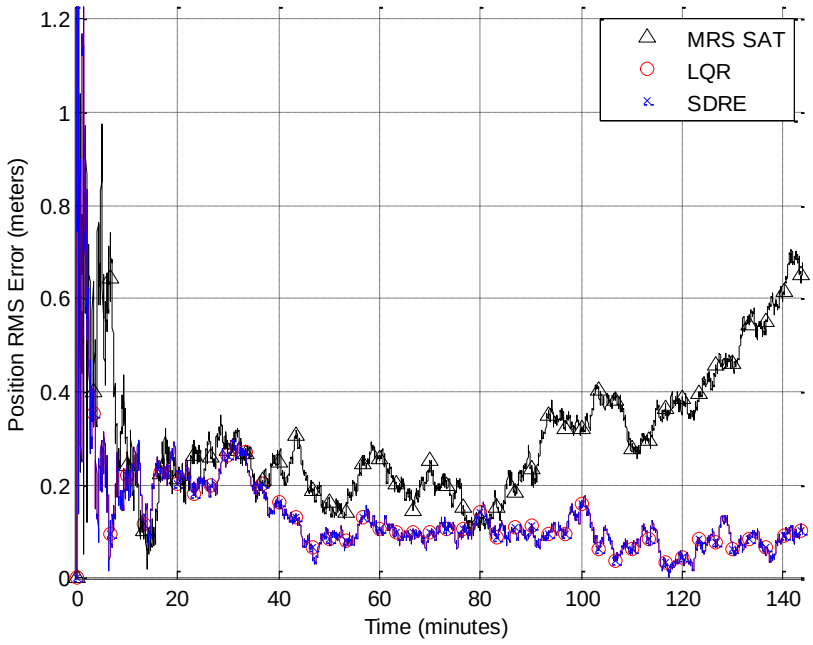

Figure 4.7. Root Mean Square Position Estimate Error

The position error in each axis should oscillate about zero or asymptotically approach zero to ensure a steady state estimate error. Figure 4.8 shows the error between the state estimate and the true states as a function of time along the three principle axes.

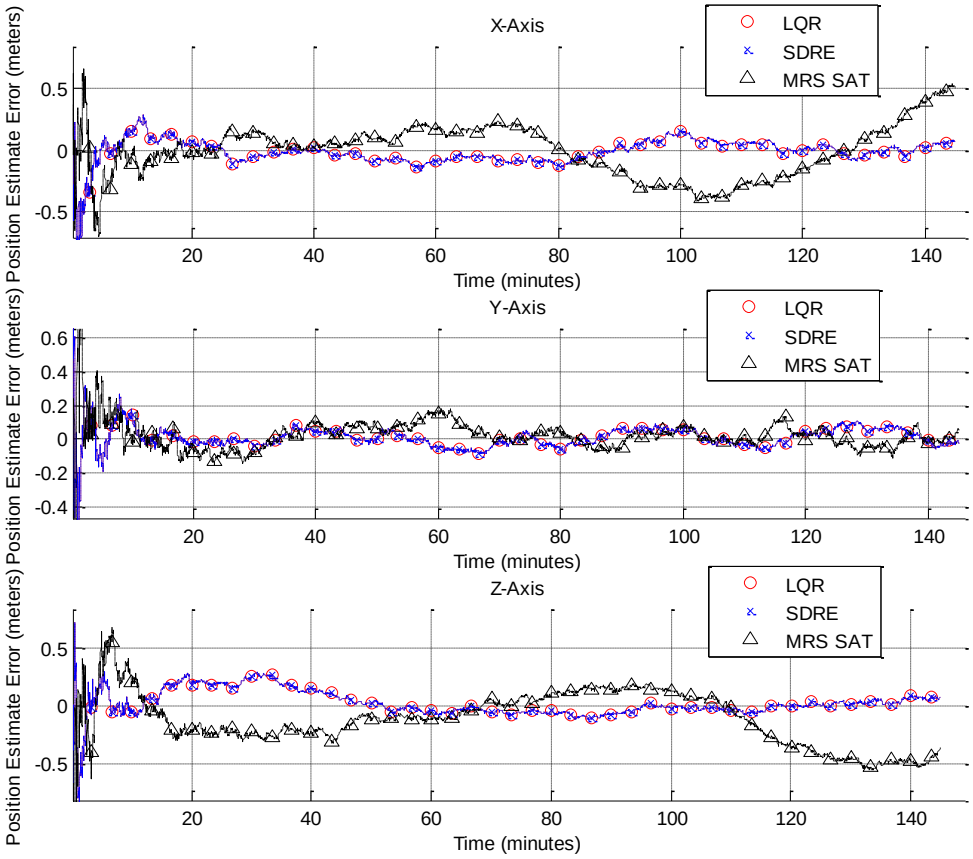

Figure 4.8. Principle Axis Position Estimate Error

The UKF filters the noise to an acceptable confidence level. This acceptability level is given by the M-SAT mission requirements in Table 2.2. It should be noted that the 3σ error bounds are not plotted because the errors do not approach this boundary in a significant way. The state estimate oscillates about the zero value for estimate error along each axis.

The determining factor in the amount of noise that can be accepted by the system is RMS position error and the velocity change profile. The RMS position error and the velocity change profile for the noisy states are plotted with the noiseless simulation of the same parameters. Figure 4.9 illustrates the effect that noise has on the root mean square tracking error.

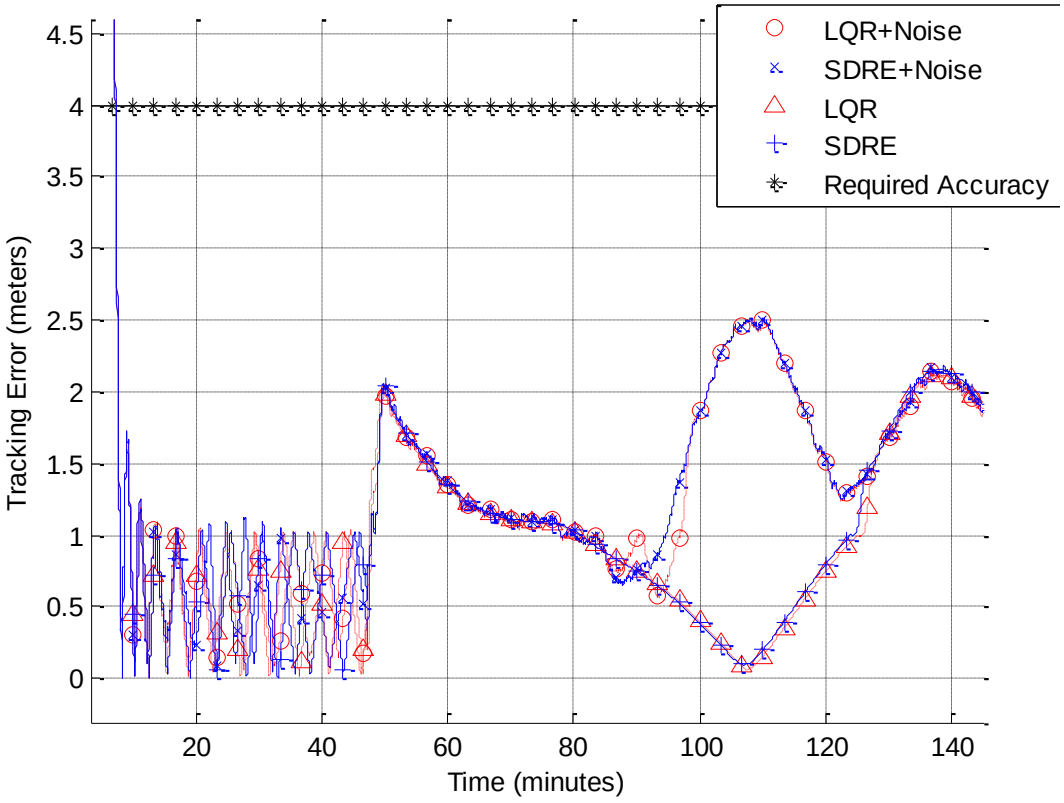

Figure 4.9. Tracking Error For Nominal and Noisy Scenarios

It can be observed that there is a significant increase in both controller's target path deviation. The deviations specifically occur during the last portion of the circumnavigation. Drift caused by nonlinear effects (which are not accounted for in the

control free path derivation) have to be corrected. These errors affect both controllers similarly, however the effect does not cause a violation of the mission success criteria. Figure 4.10 illustrates the difference between the nominal tracking error and the tracking error in the noisy scenario.

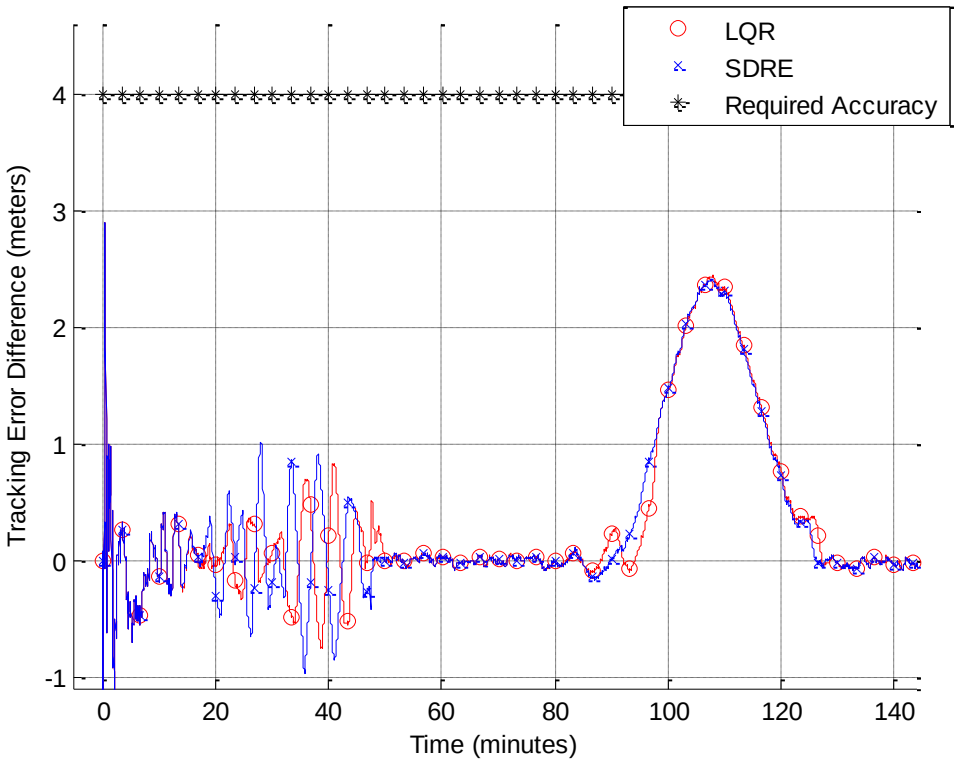

Figure 4.10. Tracking Error Difference for Nominal and Noisy Scenarios

A noisy environment affects the ability of the LQR and SDRE controllers to track the target position. The velocity change profile is also important to observe when evaluating the effects that measurement noise may have on the system. Figure 4.11 shows the cumulative velocity change for the nominal and noisy cases.

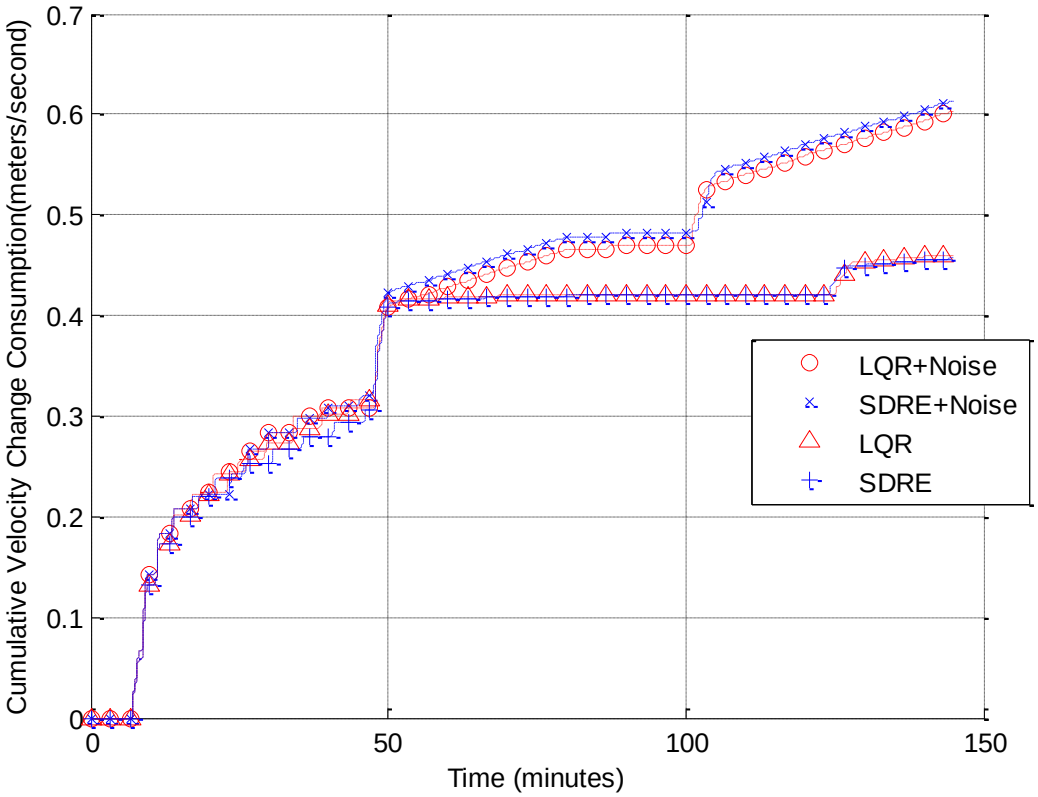

Figure 4.11. Velocity Change Variation with Noise

After transitioning to the circumnavigation maneuver, the velocity change profile changes more significantly. Figure 4.12 shows the difference between the velocity change for the nominal and noisy cases for the LQR and SDRE controllers.

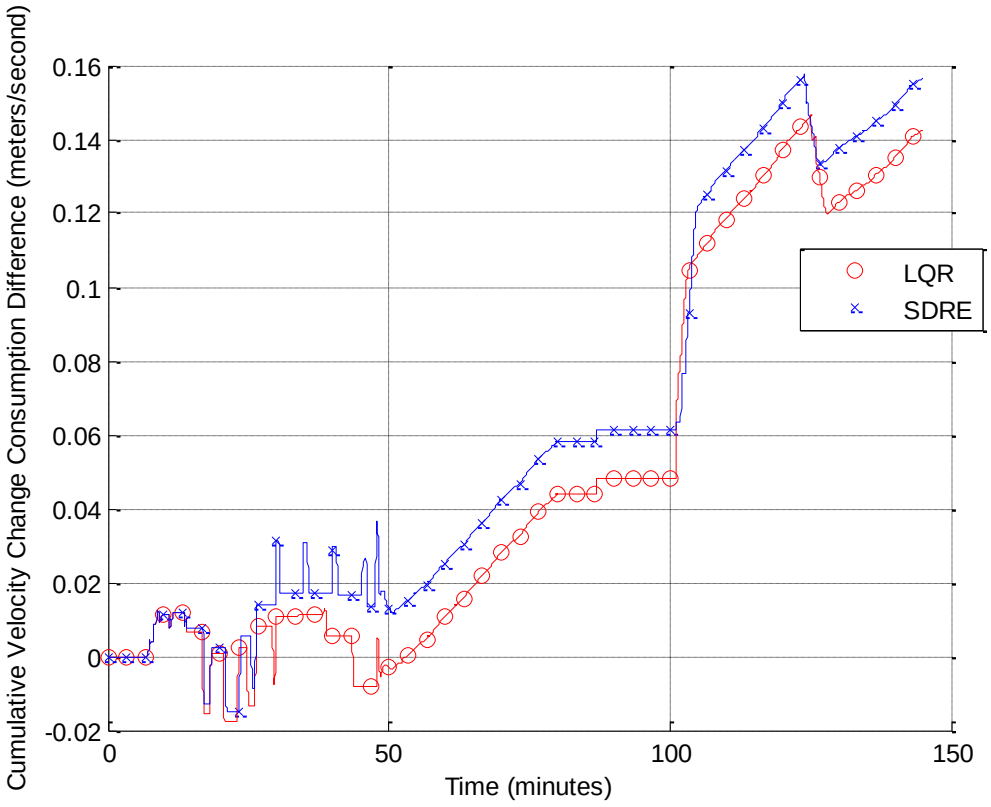

Figure 4.12. Cumulative Velocity Change Difference, n = 5

The cumulative velocity change increases by twenty percent when noise is added to the simulation. The noise addition causes an increase in velocity change for both controllers; however, the SDRE and LQR controllers are both affected similarly.

Using the results from the n = 5 case, it is known that the measurement noise causes inefficiencies for the M-SAT mission, most specifically in the velocity change required to perform the mission.

4.3.2. High Noise Case Study. It is pertinent to determine at what value the measurement noise causes the M-SAT mission requirements to be violated. The value of $\boldsymbol{n}$ is increased to a worst case scenario of $\boldsymbol{n = 25}$. This corresponds to a white noise equivalent of the circumnavigation distance. Figure 4.13 shows the LQR and SDRE tracking errors for the nominal case and the worst-case scenario.

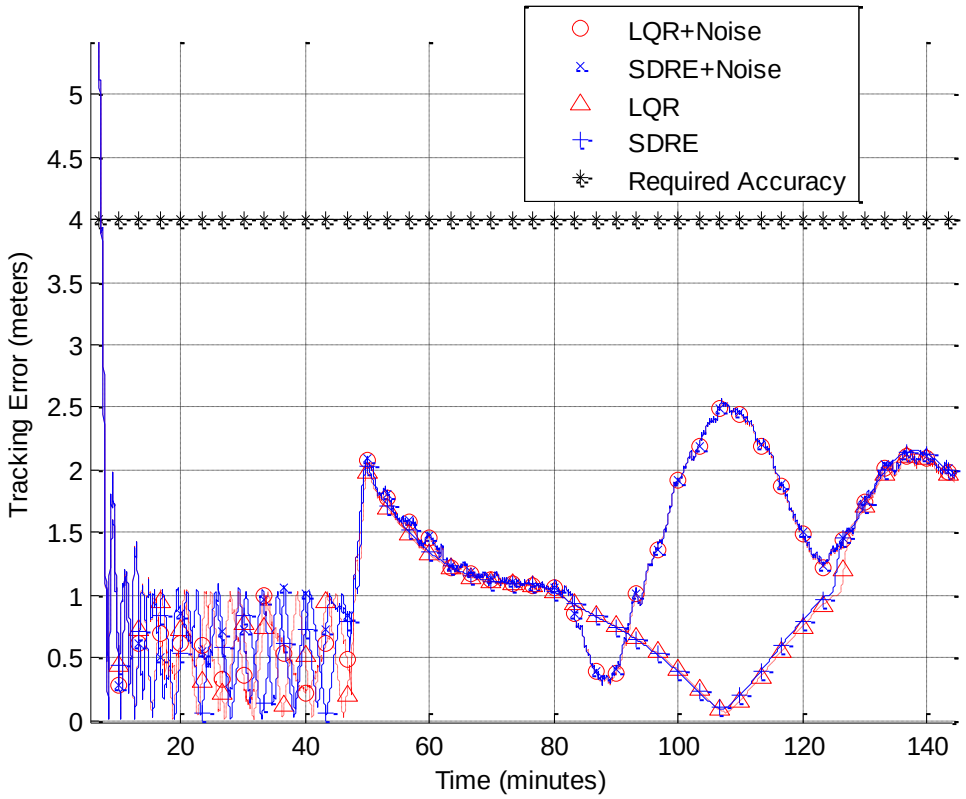

Figure 4.13. Tracking Error for Nominal and Worst-Case Noise Scenario

The tracking error is not altered significantly by the addition of noise between $n = 5$ and $n = 25$. Figure 4.14 shows the velocity change for the nominal and worst-case scenarios for the LQR and SDRE controllers. There is a well-defined increase in the velocity change for the LQR and SDRE controllers. The most significant increase comes from the circumnavigation maneuver portion of the mission. The difference in velocity change between the nominal and worst-case scenarios is illustrated in Figure 4.15.

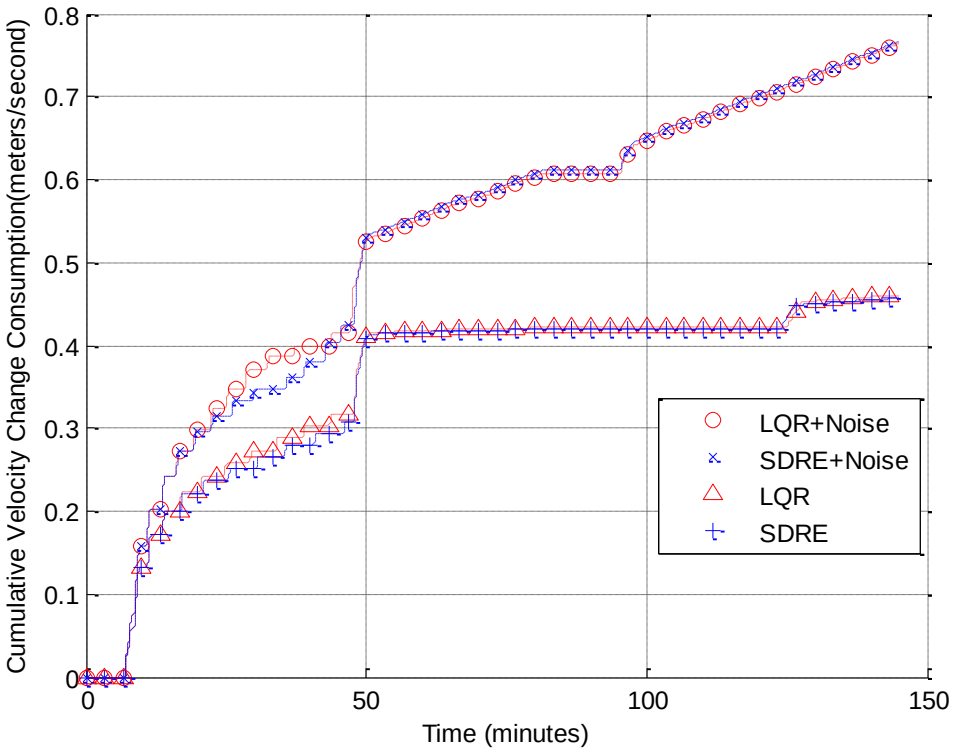

Figure 4.14. Velocity Change for Nominal and Worst Case Scenarios

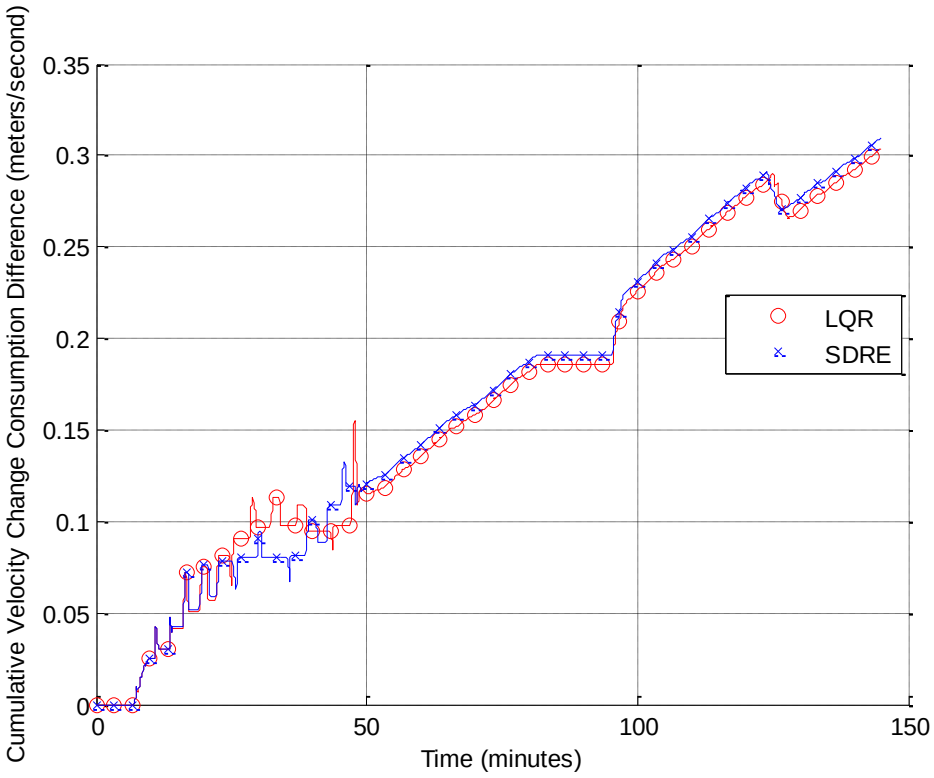

Figure 4.15. Cumulative Velocity Change Difference, n = 25

A significant velocity change occurs between the nominal and worst-case noise scenario. In order to observe how this velocity change is manifested, it is pertinent to observe the control saturation and control commands for the LQR and SDRE control algorithms in the worst-case noise scenario, as illustrated by Figure 4.16. The control saturation points increase when compared to the nominal thrust profile for the M-SAT mission. The control saturation peaks are more frequent, and the control is saturated at six points. The main increase in velocity change comes from the circumnavigation phase. As can be seen, a continuous, oscillatory low thrust is commanded during the circumnavigation. This is caused by the MR SAT state estimate falling outside the dead-band region resulting in the spacecraft attempting to correct this erroneous position, and, subsequently, requiring additional maneuvering, leading to inefficiencies. Increasing the measurement noise increases the velocity change, however does not affect the tracking error significantly. Increasing the measurement noise also affects the LQR and SDRE controllers similarly and thus does not indicate a preference of one versus the other.

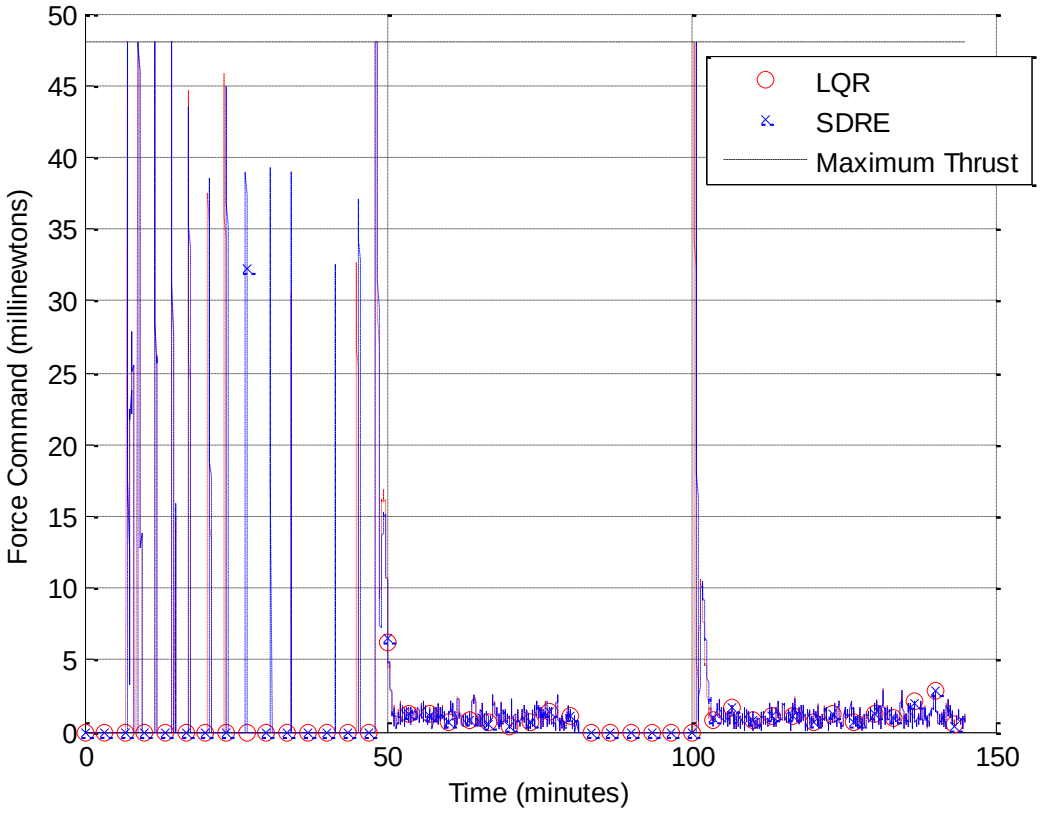

Figure 4.16. Commanded Control, n = 25

5. CONCLUSION AND FUTURE WORK

This thesis describes the mission requirements and outlines a mission plan for spacecraft separation, formation stabilization, and RSO circumnavigation over a 1.5 orbital period time frame. Autonomous path design and comparisons of multiple feedback control systems are developed as a preliminary investigation into the M-SAT mission. The effects of data corruption with measurement and process noise on the mission success criteria are also investigated to determine the performance requirements of the onboard state sensors. The results presented provide a basis for simulating the M-SAT mission from separation to extended life tests. Velocity change and fuel consumption rates are provided for future mission design and requirement verification. It is determined that for this specific application and particular hardware assembly, a linear control algorithm provides similar performance when compared to a nonlinear controller with the assumptions made. The maximum measurement noise that is allowable for the M-SAT mission to meet the mission requirements is dependent on the amount of velocity change that is willing to be sacrificed. A balance must be accomplished which weighs velocity change against vision-based navigation measurement noise levels. This study is intended to determine the separation distance, inspection path design, perform an initial controller comparison and determine the maximum measurement noise allowable for a vision-based navigation system.

Future work intends to pursue other guidance and control schemes to perform the M-SAT mission. A more robust path definition scheme and mission plan is desired in order to improve the confidence in the autonomous algorithms to compensate for unknown perturbations or defects which may be unknown at launch. Investigation into an adaptive control scheme where autonomous corrections can be made to account for pointing errors, thruster misalignment, and thrust inefficiencies is desired. Analysis into the effects that pointing and thruster errors may have upon the mission success and requirements is also desired to achieve a better measure of the effects of error accumulation on velocity change.

A higher fidelity model is also desired to incorporate more perturbations. Analysis over a wide range of possible orbits is also needed to determine the effects that various

initial conditions (orbit inclination, eccentricity, longer orbit periods etc.) have on the velocity change and target path deviation. Finally, incorporation of attitude control algorithms would be an important step in defining the total velocity change required for the M-SAT mission (noting that the cold gas system performs both orbit and attitude control).

A Monte-Carlo approach as a method to analyze the affects of measurement noise on the control algorithms is desired. This method would run each noise scenario multiple times and average the resulting position and velocity to provide a mean approximation to the actual on orbit environment.

REFERENCES

[1] Department of Defense, "*Defense Technology Area Plan*," 2000, VIII-14.

[2] NASA, "Overview of the DART Mishap Investigation Results", 2006.

[3] Clohessy, W.H. and Wiltshire, R.S., "Terminal Guidance for Satellite Rendezvous", *J. Aerospace Sciences*, Vol. 27 (1960), p 653.

[4] D'Amico, S. and Montenbruck, O., "Proximity Operations of Formation-Flying Spacecraft Using and Eccentricity/Inclination Vector Separation," *Journal of Guidance, Control, and Dynamics*, Vol. 29, No. 3, 2006.

[5] Alfriend, K., and Schaub, H., "Dynamics and Control of Spacecraft Formations: Challenges and Some Solutions," *Journal of Astonautical Sciences*, Vol. 48, No. 2-3, 2000, pp. 249-267.

[6] Vadali, S.R., Schaub, H., and Alfriend, K.T., "Initial Conditions and Fuel-Optimal Control for Formation Flying of Satellites," AIAA Paper 99-4265, AIAA GNC conference, Portland, OR, 1999.

[7] Armellin, R., Massari, M., and Finzi, A.E., "Optimal Formation Flying Reconfiguration and Station Keeping Maneuvers Using Low Thrust Propulsion," *18th International Symposium on Space Flight Dynamics*, Munich, Germany, 2004.

[8] Harl, N., and Pernicka, H.J., "Low-Thrust Control of a Lunar Mapping Orbit", *Journal of Guidance, Control and Dynamics*, 2009, Vol. 32, No. 2, pp. 939-948.

[9] M.J. Patterson, "Low-Power Ion Propulsion for Small Spacecraft," National Aeronautics and Space Administration, Lewis Research Center, Cleveland, Ohio, 1997.

[10] Eyer, J.K., "A Dynamics and Control Algorithm for Low Earth Orbit Precision Formation Flying Satellites," Ph.D. Dissertation, Graduate Department of Aerospace Science and Engineering, University of Toronto, 2009.

[11] Phelps,T.K., Wiseman, S., Komm, D.S., Bond, T., Pinero, L.R., "Development of the NEXT Power Processing Unit," 39th Joint Propulsion Conference and Exhibit, Huntsville, Alabama, July 20-23, 2003.

[12] Dancer, M.W., Searcy, J.D., and Pernicka, H., "Orbit/Attitude Determination and Control for the UMR SAT Mission," 21st Annual AIAA/USU Conference on Small Satellites, Logan, Utah, August 13-16, 2007.

[13] Xin, M. and Balakrishnan, S. N., "A New Method for Suboptimal Control of a Class of Nonlinear Systems," *Journal of Optimal Control Applications and Methods,* Vol. 26, 2005, pp. 55-83.

[14] Bo J. Naasz, "Classical Element Feedback Control for Spacecraft Orbital Maneuvers," M.S. Thesis, Graduate Department of Aerospace Engineering, Virginia Polytechnic Institute, 2002.

[15] Vasser, R. H. and Sherwood, R. B., "Formationkeeping for a Pair of Satellites in a Circular Orbit," *Journal of Guidance, Control, and Dynamics*, Vol. 8, No. 2, 1985, pp. 235-242.

[16] S.R. Starin, R.K. Yedavalli and A.G. Sparks, "Design of a LQR Controller of Reduced Inputs for Multiple Spacecraft Formation Flying," *Proceedings of the American Control Conference,* Arlington, VA, June 25–27, 2001.

[17] Saenz-Otero, A., Miller, D.W., "The SPHERES ISS Laboratory for Rendezvous and Formation Flight," 5th International ESA Conference On Guidance, Navigation and Control Systems, Frascati, Italy, 22-25 October 2002, Paper #29.

[18] Kristiansen, R. and Nicklasson, P.H., "Spacecraft Formation Flying: A Review and New Results on State Feedback Control," *Acta Astronautica*, Vol. 65, Issues 11-12, 2009, pp.1537-1552.

[19] Vallado, D.A. and McClain, W.D., *Fundamentals of Astrodynamics and Applications*, 3rd ed., Microcosm Press/Springer, 2007.

[20] J. R. Wertz and R. Bell, "Autonomous Rendezvous and Docking Technologies — Status and Prospects," Space Systems Technology and Operations Conference, Orlando Florida, April 21-25, 2003.

[21] C. D'Souza, F. C. Hanak, and P. Spehar, "Orion Rendezvous, Proximity Operations, and Docking Design and Analysis," AIAA Guidance, Navigation and Control Conference and Exhibit, Hilton Head, South Carolina, 20-23 Aug. 2007, AIAA 2007-6683.

[22] M. F. Machula and G. S. Sandhoo, "Rendezvous and Docking for Space Exploration," 1st Space Exploration Conference: Continuing the Voyage of Discovery, Orlando, Florida, Jan. 30-Feb. 1, 2005, AIAA 2005-2716.

[23] J. L. Goodman, "History of Space Shuttle Rendezvous and Proximity Operations," *Journal of Spacecraft Rockets*, Vol. 43, No. 5, Sep.-Oct. 2006, pp. 944-959.

[24] R. Quitero, R. C. Montgomery, and P. Tchoryk, "Autonomous Rendezvous and Docking Scenarios for The Development of Guidelines and Standards," AIAA Space Programs and Technologies Conference and Exhibit, Huntsville AL, Sep. 21-23, 1993, AIAA 93-4753.

[25] W. S. Cook and S. D. Lindell, "Autonomous Rendezvous and Docking (AR&D) for Future Spacecraft Missions," AIAA Space Technology Conference & Exposition, Albuquerque, NM, Sep. 28-30, 1999, A99-42136.

[26] T. Carrico, T. Langster, J. Carrico, D. Vallado, M. Loucks, and S. Alfano, "Proximity Operations for Space Situational Awareness: Spacecraft Closed-Loop Maneuvering Using Numerical Simulations and Fuzzy Logic," Advanced Maui Optical and Space Surveillance Technologies Conference, Sep. 2006.

[27] M. E. Polites, "Technology of Automated Rendezvous and Capture in Space," *Journal of Spacecraft and Rockets*, Vol. 36, No. 2, Mar.–Apr., 1999.

[28] P. Singla and K. Subbarao, "Adaptive Output Feedback Control for Spacecraft Rendezvous and Docking Under Measurement Uncertainty," *Journal of Guidance, Control, and Dynamics*, Vol. 29, No. 4, Jul-Aug 2006.

[29] Seubert, Carl Reiner, "Refrigerant-Based Propulsion System for Small Spacecraft," M.S. Thesis, University of Missouri-Rolla, 2007.

[30] Pahl, Ryan Alan, "Integration and Test of a Refrigerant-Based Cold-Gas Propulsion System for Small Satellites," M.S. Thesis, Missouri University of Science and Technology, 2010.

[31] Lee, Daero, "Guidance, Navigation and Control System for Autonomous Proximity Operations and Docking of Spacecraft," Ph.D. Dissertation, Missouri University of Science and Technology, 2009.

[32] Damaren, C.J., "Almost Periodic Relative Orbits Under J_2 Perturbations," *Proceedings of the Institution of Mechanical Engineers, Part G: Journal of Aerospace Engineering*, Vol. 221, No. 5, 2007.

[33] Julier, S.J., Uhlmann, J.K., "A New Extension of the Kalman Filter to Nonlinear Systems," The Robotics Research Group, Department of Engineering Science, The University of Oxford, 1997.

VITA

The author, James Harris Meub, was born December 24, 1986. He earned his Bachelor of Science degree in Aerospace Engineering from Missouri University of Science and Technology in May 2009. This thesis is presented to fulfill the requirements for Master of Science in Aerospace Engineering at Missouri University of Science and Technology, was awarded in May 2011.